Laser Powder Bed Fusion (LPBF) of a Complex Aerospace Component: Effects of Layerwise Process Control on Part Quality

by

David Paul Spadaccia

Thesis submitted to the faculty of the Virginia Polytechnic Institute and State University in partial fulfillment of the requirements for the degree of

Master of Science

In

Mechanical Engineering

Christopher B. Williams, Chair

Prahalada K. Rao, Co-Chair

Robert L. West

May 28, 2025

Blacksburg, Virginia

Keywords: Additive Manufacturing, Laser Powder Bed Fusion, Process Control, Topology Optimization





This research is funded by the following grants awarded to the thesis advisors, Dr. Prahalada Rao and Dr. Chris Williams from the various federal agencies of the United States government.
National Institute of Standards and Technology (NIST)
National Science Foundation (NSF)
Office of Naval Research (ONR)
Department of Defense (DoD)

NSF CMMI 2309483/1752069
CAREER: Smart Additive Manufacturing
Fundamental Research in Sensing, Data Science, and Modeling Toward Zero Part Defects

NSF PFI-TT 2322322
Ultrafast Thermal Simulation of Metal Additive Manufacturing

NIST 70NANB23H029T
Predicting flaws in LPBF by combining thermal simulations with in-situ sensor data

US Department of Defense, Office of Naval Research (ONR)
National Defense Education Program (NDEP) for Science, Technology, Engineering, and Mathematics (STEM) Education, Outreach, and Workforce Initiative Programs under Grant No. HQ0034231004.

FAIM: Future Additive Interdisciplinary Manufacturing

ONR N00014-21-1-2781
Designing and 3D Printing Alloys

Laser Powder Bed Fusion (LPBF) of a Complex Aerospace Component: Effects of Layerwise Process Control on Part Quality

David Spadaccia

Abstract

This research concerns the laser powder bed fusion (LPBF) metal additive manufacturing (AM) process. The ***goal*** is to optimize critical processing parameters for a complex LPBF part. Currently, LPBF process qualification relies on empirical parameter experiments and rigorous materials characterization. Once applied to end-use, complex geometries, this process can take over 2 years of engineering effort and more than $4 million dollars.

Further, empirically-determined process parameters often do not scale to complex parts without expensive supporting structures required to maintain a stable manufacturing process. During the LPBF process, the part is subjected to continual heating and cooling cycles. This thermal history governs every aspect of the part's quality, from its microstructure, defects, geometric accuracy, residual stresses, and ultimately, determines its functional properties. Hence, controlling the thermal history is critical for obtaining high quality LPBF parts.

Accordingly, the ***objective*** of this work is to evaluate part quality, thermal history, and support structure optimization of process-controlled parts to compare against their nominally printed counterparts. This approach leverages a feedforward thermal history control algorithm known as DynamicPrint for LPBF of a complex aerospace component (GE bracket) made from Inconel 718 material. This approach, which is a form of model predictive feedforward control, uses a physics-based model to autonomously adjust processing parameters layer-by-layer *before* the part is printed to avoid heat build-up and thermal history excursions during printing.

This research tests and affirms the ***hypothesis*** that controlling the thermal history via layerwise modulation of laser power and velocity improves part quality. This thesis evaluates and compares the quality of thermal history-controlled LPBF parts against parts printed with empirically optimized, constant process parameters. Compared to uncontrolled parts, process-controlled parts show improved dimensional accuracy and reduced thermal-induced warping. Specifically, compared to parts produced under fixed, nominal conditions, layerwise control eliminated distortion defects and reduced necessary support structure volume by 45%.

This work demonstrates a scalable approach for applying layerwise thermal history process control to a complex geometry, where a key challenge in practical LPBF applications lies in dynamically modifying process parameters to accommodate complex geometries. Notably, this method enables rapid, autonomous optimization of process conditions in LPBF – critical to accelerated part qualification – and reduces process development time from months to weeks, while fabricating better quality parts that cost less.

Laser Powder Bed Fusion (LPBF) of a Complex Aerospace Component: Effects of Layerwise Process Control on Part Quality

David Spadaccia

General Audience Abstract

This research concerns the laser powder bed fusion (LPBF) metal additive manufacturing (AM) process. The ***goal*** is to optimize process parameters for a complex LPBF part. Currently, LPBF process qualification for complex parts relies on extensive parameter experiments and rigorous material properties testing. Once applied to end-use, complex geometries, this process can take over 2 years of engineering effort and more than $4 million dollars.

Further, experimentally-determined process parameters often do not scale to complex parts without expensive supporting structures required to maintain a stable manufacturing process. During the LPBF process, the part is subjected to continual heating and cooling cycles. This thermal history governs every aspect of the part's quality, from its defects, geometric accuracy, and ultimately determines its functional properties. Hence, controlling thermal history is critical for obtaining high quality LPBF parts.

Accordingly, the ***objective*** of this work is to evaluate part quality, thermal history, and support structure reduction of process-controlled parts to compare against their nominally printed counterparts. This approach leverages a temperature control algorithm known as DynamicPrint for LPBF of a complex aerospace component (GE bracket) made from Inconel 718 material. This approach uses a physics-based model to autonomously adjust processing parameters layer-by-layer *before* the part is printed to avoid heat build-up during printing.

This research tests and affirms the ***hypothesis*** that controlling thermal history through layerwise process parameter changes improve part quality. This thesis evaluates and compares the quality of thermal history-controlled LPBF parts against parts printed with constant process parameters. Compared to uncontrolled parts, process-controlled parts show improved dimensional accuracy and reduced warping associated with overheating. Specifically, compared to parts produced under fixed, nominal conditions, layerwise control eliminated distortion defects and reduced support structure volume by 45%.

This work demonstrates a scalable approach for applying layerwise thermal history process control to a complex geometry, where a key challenge in practical LPBF applications lies in modifying process parameters to accommodate complex geometries. Notably, this method enables rapid, autonomous optimization of process conditions in LPBF – critical to accelerated part qualification – and reduces process development time from months to weeks, while fabricating better quality parts that cost less.

Acknowledgement

I extend my thanks to my committee for their time and mentorship during my studies at Virginia Tech. I thank Dr. Prahalada Rao for his advice, guidance, and motivation throughout my thesis work and for taking on a new graduate student directly after an internship. I thank Dr. Robert West for his mentorship, especially during his Finite Element Analysis course that drove interest in many simulation-focused projects. I am especially grateful to Dr. Christopher Williams, who originally inspired me to pursue my passion for additive manufacturing, accepted me as an undergrad in his lab, and opened so many doors for me in my career.

I would like to thank my many labmates throughout my undergraduate and graduate research experiences. Especially for my thesis work, I thank Kaustubh Deshmukh, Mihir Darji, Antonio Carrington Jr., Alex Riensche, Benjamin Bevans, Carson Perry, Kamden Shephard, and Hunter Goddard for their guidance, help troubleshooting, and lighthearted times together. In prior undergrad projects, I would also like to thank Tadek Kosmal, Kieran Beaumont, and Hutch Peter for their patience, teaching lessons, and fun times together.

While not at the lab, I thank my many friends who kept me sane, kept me active, and always put a smile on my face: Henry Forsyth, Mike Yanoschak, Chris Nelson, Brice Donaldson, Mitchell Davis, Tim McEvoy, Ronit Basu, Malik Deslauriers, Vivek Gopalam, Nick Eastman, Zach Moore, Kevin Hallissey, Saran Rathore, and Paul Cacioppo.

None of my success would be possible without the support of my family. I am forever grateful to my mother, Kris, for her unwavering encouragement. I thank my widespread family: Tony, Michael, Ann, Daniel, Mary “Grammy”, Lary “Grandpa”, Margaret “Nana”, Vince, Bruce, Kerri, Brian, Wendy, Zack, Matt, Chris, Lexi, Miranda, Olivia and Kate, for their love and fun times throughout my upbringing. Last but not least, I treasure my “tuxedo” cat Phoebe.

I stand on the shoulders of great men who taught me the foundational principles I carry with me today as an aspiring engineer. While not with us today, I am indebted to my grandparents: Paul “Grandpa”, whose name I bear, and Joseph Sr. “Gramps” for all the lessons, kindheartedness, and education throughout my early life. My father, Joe “Papa”, who passed during my graduate studies, was instrumental in raising me as the man I am today.

This work is fully dedicated to him in memory.

Table of Contents

Table of Figures

Table of Tables

1 Introduction

1.1 Goal, Rationale, and Objective

This research concerns the laser powder bed fusion (LPBF) additive manufacturing (AM) of metal parts. The ***goal*** of this thesis is to apply an established feedforward model predictive process control approach known as DynamicPrint [1] to a complex geometry made from a Nickel-based superalloy Inconel 718 (IN718) [2]. The standard approach for LPBF process qualification relies on an empirical trial-and-error approach for parameter development, such as laser power and laser velocity process parameters. Currently, industry estimates that qualifying a machine-material combination, excluding part-specific qualification, requires over 2 years of engineering effort and exceeds $4 million in expenses [3].

Further, the thermal history, the spatiotemporal temperature distribution during the LPBF process, is a crucial determinant of resulting part quality. Due to distinct heating and cooling mechanisms, the thermal history affects multi-scale aspects of the part including its microstructure, defects, residual stresses and build risk, and ultimately, determines its functional properties, such as its strength and fatigue life [4].

Rather than employing a build-and-test approach for a complex part, this work leverages feedforward process control to simulate a part-level thermal history to adaptively determine the process parameters based on a target thermal history. The ***objective*** of this work is to evaluate part quality, thermal history, and support structure optimization of process-controlled parts to compare against their nominally printed counterparts. While process control has been used previously in the literature to mitigate flaw formation in LPBF parts, a key gap is the lack of application to practically motivated, geometrically complex parts. This work addresses that gap by applying process control to a strength-optimized aerospace part.

1.2 Background of the Laser Powder Bed Fusion (LPBF) Process

1.2.1 Process Basics

LPBF is an AM process in which metal powder is recoated onto a build plate and selectively melted in a layer-wise fashion using a fast-moving, high-energy laser. A schematic of a standard LPBF machine is shown below in Figure 1-1. Typically, an LPBF machine uses an infrared Nd:YAG fiber laser (wavelength 1064 nm), with laser power ranging from 200 W to 500 W, laser spot size ranging from 50-100 μm, and laser velocity ranging from 500 to 1000 mm/s to scan a thin (30-50 μm) layer of metal powder [5]. The laser is translated across the build plate by a galvanometric mirror assembly, and focused onto the build plate by means of an f-θ or variable-focus lens system [6]. Prior to printing, the chamber is purged to reduce oxygen levels below 0.10%. Depending on the material processed, the chamber is filled with Argon or Nitrogen gas with pressures typically ranging from 90-100 kPa [7], [8].

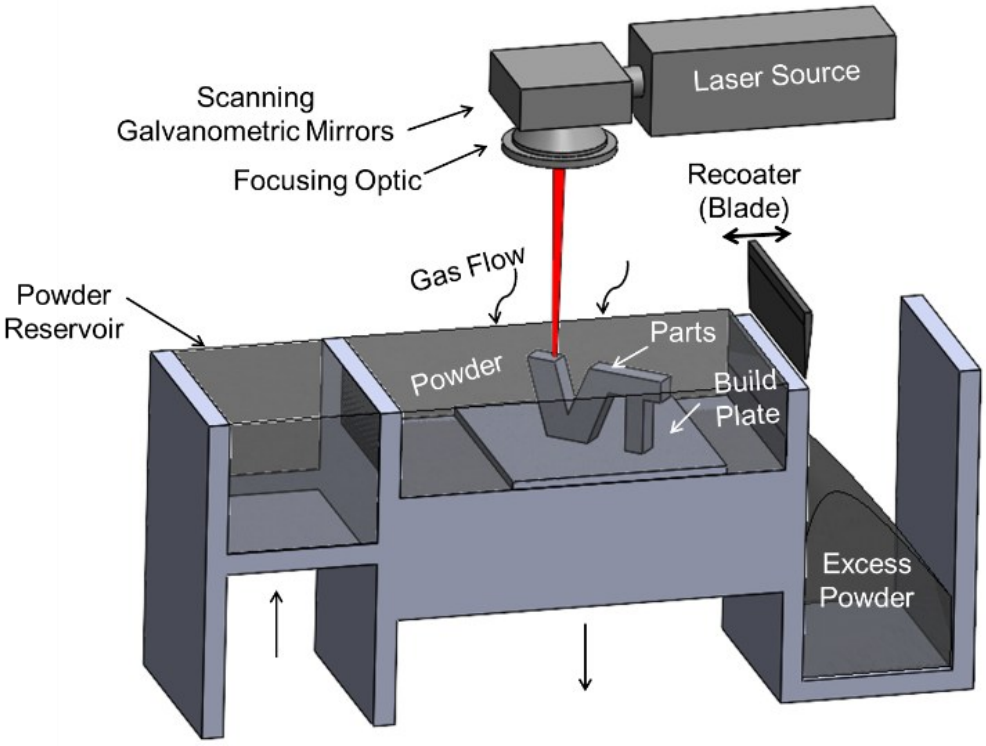

Figure 1-1: Example LPBF machine diagram [9]

LPBF can produce parts with high-performance metal alloys of Iron (stainless steel 316L, stainless steel 17-4 PH, maraging and tool steels), Titanium (Ti6Al4V), Nickel (Inconel 718, 625) and Cobalt (CoCr) [10]. Typical production rates range from 20-90 cm^3/hour [11], with dimensional accuracy within 20 to 100 μm [12], and average surface roughness (Ra) exceeding 10 μm [13]. Maximum part size range depends on machine build volume, ranging from 125 × 125 × 125 mm (small) to 300 × 300 × 300 mm (medium), and over 600 × 600 × 600 mm for industrial-scale production machines. Recently, market-available LPBF systems with as many as 12 lasers have been introduced to increase production rates [14].

1.2.2 Applications

Especially in the aerospace industry, LPBF has seen increasing adoption due to its ability to create flight- and space-qualified metal parts with complex geometries not afforded by traditional manufacturing techniques [15, 16]. A main benefit of LPBF is its wide range of part and feature scales combined with the geometric freedom similarly afforded among other AM processes. Its relatively small minimum feature size enables high-resolution, thin-walled geometries and interior channels and a maximum part scale competitive with other metal AM processes [17, 18]. One example of LPBF-enabled complex geometries includes Topology Optimization (TO), where a material distribution is algorithmically optimized within a pre-defined domain [19, 20]. The designs created from TO studies are often complex, and are thus suitable candidates for AM [21]. As shown in Figure 1-2, examples are given for TO geometries enabling improved performance owing to the combination of design optimization and the design freedom offered by LPBF. In Figure 1-2(a), a structurally-optimized spacecraft bracket geometry which achieved a technology readiness level (TRL) of five through validation testing, 67% mass reduction, and 135% increased rigidity. In Figure 1-2(b), an automotive brake caliper was structurally optimized to achieve 41.6%

mass reduction and front/rear displacement reductions of 59.3% and 17.1%, respectively. Figure 1-2(c) shows a molding application where cooling channels are thermally optimized to promote a 43% reduction in temperature standard deviation. Finally, in Figure 1-2(d), a moth class sailing boat rudder bulb was structurally- and fluid-optimized to achieve 58% mass reduction and reduced drag force of 19.9% through biomimetic fish scale geometries.

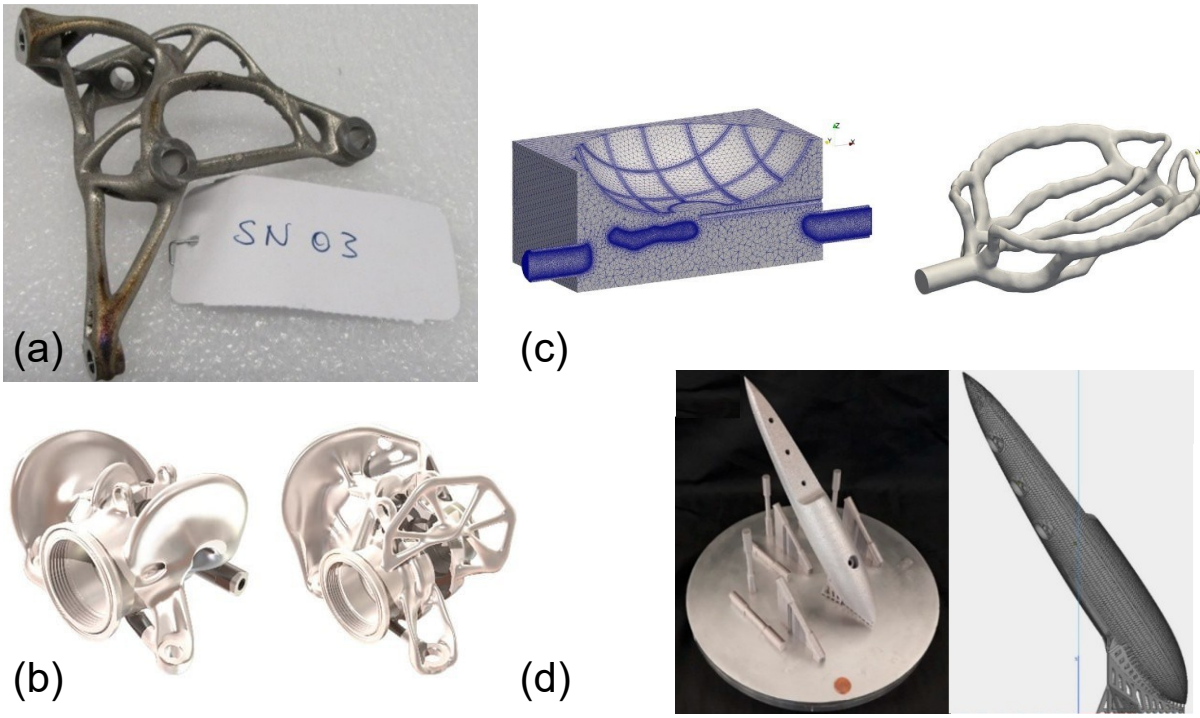

Figure 1-2: Examples of LPBF-enabled TO geometries. (a) Ti-6Al-4V bracket for space applications with 67% reduction in mass [22]. (b) 18Ni-300 maraging steel die casting insert with interior cooling channels achieving 43% reduction in temperature standard deviation [23]. (c), Ti-6Al-4V brake caliper with maximum displacement reductions of 59.3% (front) and 17.1% (rear) with total weight savings of 41.6% [24]. AlSi7Mg0.7 sailing boat rudder bulb achieving 58% mass reduction, reduced drag force of 19.9% [25].

1.2.3 Gaps and Challenges

While LPBF affords an enhanced design freedom of end-use, high-performance metal parts, there exist manufacturing-specific considerations that can inhibit part quality and cause build failures. For example, features with steep overhangs (< 45° with respect to the horizontal), even with optimized process parameters, incur excessive upward distortion, which can lead to recoater collisions, recoater blade damage and unevenly recoated powder layers, causing further geometric deviation [26]. To overcome this issue, practitioners can regulate the LPBF process by introducing supporting structures to mechanically anchor a part and better transfer heat away from the part. However, by introducing supporting structures, the costs associated with additional printing time, material, and subsequent removal of these structures greatly increases manufacturing time and expense, inhibiting LPBF adoption [27].

Due to the laser-driven nature of LPBF, residual stresses are generated by rapid heating and solidification mechanisms: the origin of cracking and distortion in LPBF is high temperature gradients [28]. So, to reduce part defects, such as the aforementioned issue of part warpage, each part's thermal history and directly related mechanical behavior must be controlled [29]. One approach is to use thermal models, where overheating regions may correlate to future build issues. As such, the crux of LPBF is determining an acceptable thermal history. However, to comprehensively capture the thermal history of the LPBF process, the wide range of process feature scales – the laser spot size (tens of microns), the part size (centimeters), thermal gradients (~10,000 K/s), and laser scan speed (~1000 mm/s) – necessitate a prohibitively expensive computation burden [30]. Instead, reduced-order modelling is commonly used to compute a high-fidelity thermal history at an acceptable computational cost to inform future part design and part parameter decisions [31].

There are three primary approaches to regulate the thermal history of an LPBF part: (i) sensor-based feedback control [32], (ii) model-based feedforward control [33], and (iii) empirical-based approaches [34]. Through use of an automated controller or semi-automated model, a process control approach enables improvement at multiple feature scales of the LPBF process [35]. At the smaller scale, meltpool control could be used for improving surface roughness or part tolerances [36], whereas at the part scale, global temperatures could be controlled to stabilize overheating regions and mitigate excessive distortion [37]. Another key benefit of process control is its enabling of adaptive parameter selection through automatic, controller-determined parameters or through model-informed parameters. It is well known that LPBF process parameters are not geometry-agnostic, so process control facilitates part-specific parameter development by circumventing costly, empirical parameter studies [38].

While process control holds great promise for advancing current limitations of LPBF, practical part- and geometry-specific considerations remain. The chief difficulty with process control for practical LPBF applications is the increasing complexity of part geometries [39]. Despite extensive parameter optimization studies, standardized geometries' parameters fail to capture the full geometrical complexity of parts. These studies aim to remove geometrical effects on parameter quality metrics, however, an acceptable parameter window for one geometry may not be as repeatable for a more complex part geometry [32]. For instance, small-scale overhangs or thin wall features necessitate fine meltpool control due to locally changing heat conduction boundary conditions [40]. Moreover, at the part scale, maintaining a consistent thermal history is essential to homogenize as-printed microstructure and material properties [41].

1.3 Hypothesis and Novelty

This work tests the hypothesis that parts manufactured with layerwise thermal history control demonstrate higher part quality than their nominally printed counterparts. For this work, a baseline, complex geometry is chosen, then several builds are conducted to evaluate part quality and thermal history across varying support levels for process-controlled and nominally printed part pairs.

Implementation and layerwise optimization of the processing parameters is achieved through a model predictive control algorithm termed DynamicPrint as described in prior publications by this research group [1, 37]. We note that unlike real-time feedback control, the layerwise processing plan in this work is determined before the part is actually printed – a form of digital feedforward control. Previously, the model predictive feedforward process control algorithm (DynamicPrint) was applied to relatively simple geometry exemplar parts. The novelty of this work is that it adopts the DynamicPrint approach to a more complex, practical aerospace-inspired geometry with steep overhang angles and fine, curved features [1].

For this work, a baseline, topology-optimized complex geometry part is chosen. Then, several builds are conducted to evaluate part quality and thermal history across various controlled and uncontrolled builds. The geometry chosen for this project is Dr. Thomas Johansson's 2nd-place winning submission [42] to the popular GrabCAD GE jet engine bracket challenge, where contestants submitted lowest-weight, TO-generated parts given a set of load cases, boundary conditions and material properties [43]. This part was chosen for this project for its complex geometry as demonstrated in Figure 1-3, noting its thin walls, steep overhangs, and curved features.

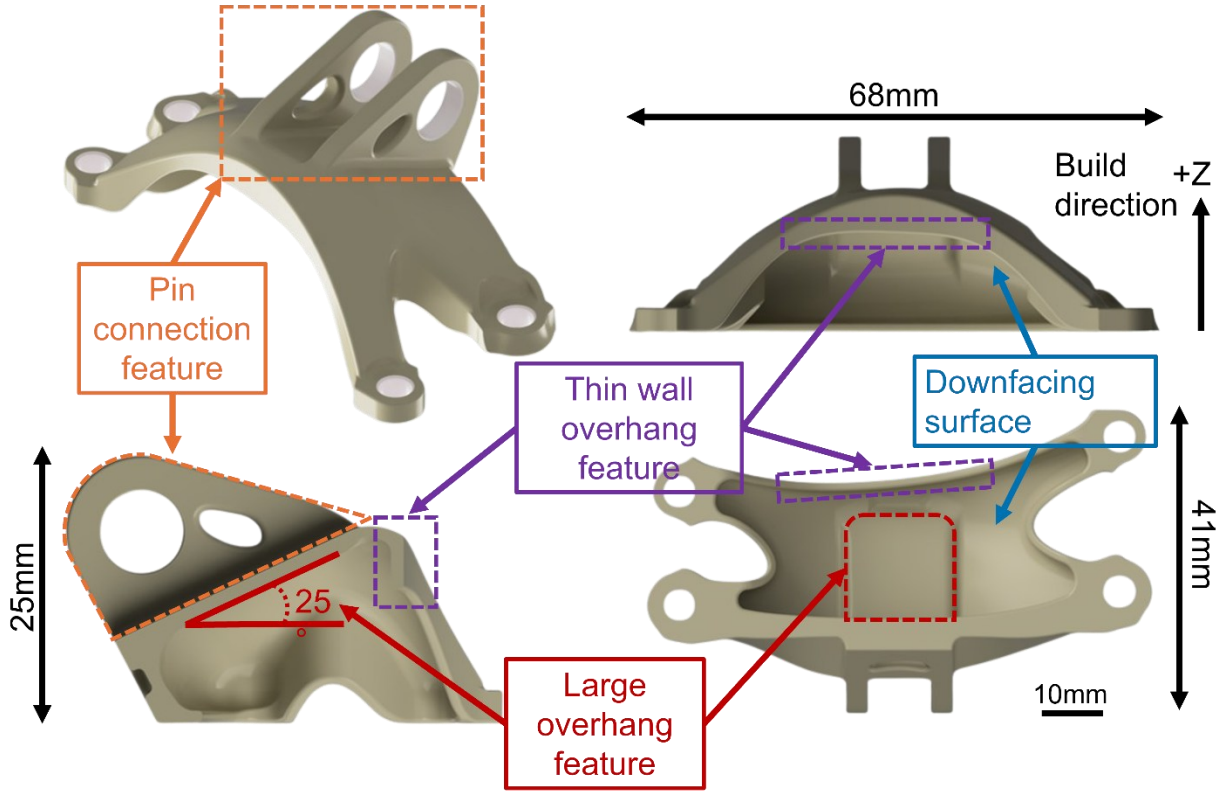

Figure 1-3: Dr. Thomas Johansson's 2nd place winning submission to the GE jet engine bracket challenge, achieving 82% weight reduction [42].

1.4 Summary of the Research Approach

A phased experimental design framework is implemented. First, an acceptable laser power (P, [W]) and velocity (V, [mm/s]) parameter window is determined through a design of experiments (DOE) build with a simple cylindrical pin geometry. The aim of this build is to identify a laser power-velocity (PV) window where lack-of-fusion, keyhole, and spatter-induced porosity regimes are nominally absent. The down-selected PV combinations define the upper and lower bounds to avoid lack-of-fusion porosity at low energy input and keyhole porosity at high energy input parameter sets. These porosity-acceptable PV sets are then used as the input choices for subsequent feedforward process control. So, given a range of PVs, a lower, Linear Energy Density ($E_L = P/V$) may be chosen for layers of overheating, whereas nominal parameters may be chosen for features with acceptable heat conduction.

In the second phase of experiments, the GE bracket is manufactured with three support strategies: unsupported, partially supported, and fully supported. The unsupported and partially supported parts are printed at both nominal and DynamicPrint process-controlled conditions. The fully supported part does not require process control; instead, it offers a baseline comparator for part quality and thermal history. All 5 parts are manufactured on a SLM 280 2.0 LPBF system at a 2:5 reduced scale using TruForm 718-35 powder material. This material is commonly referred to as Inconel 718; it is a Nickel-based superalloy that finds widespread use in aerospace applications, owing to its high strength and corrosion resistance at high temperatures [44]. The feedforward control of the thermal history is based on a mesh-free, rapid part-level thermal history simulation model. The approach has been experimentally validated with in-situ infrared thermal imaging data as detailed in several prior publications [1, 4, 37, 45-49]. Table 1-1 pictorially outlines the build plans for this work.

Table 1-1: The six outlined builds, each with a sample build layout image, and rationale.

Build Name	Build Layout	Rationale
Porosity Design of Experiments (DOE)		Determine porosity-acceptable power and velocity sets for process-controlled builds
Unsupported, uncontrolled GE bracket build		Evaluate unsupported part at nominal conditions. Compare to process-controlled counterpart.
Fully supported, uncontrolled GE bracket build	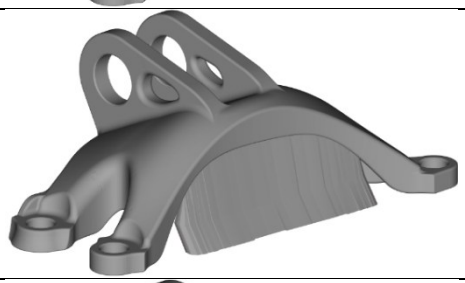	Evaluate fully supported part at nominal conditions. Compare to process-controlled builds.
Partially supported, uncontrolled GE bracket build	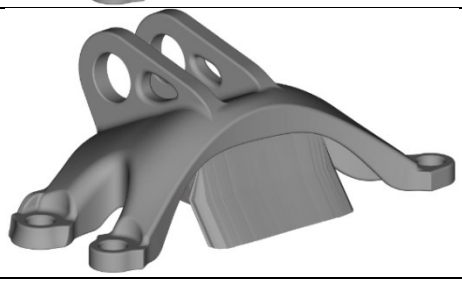	Evaluate partially supported part at nominal conditions. Compare to process-controlled counterpart.
Partially supported, process-controlled GE bracket build	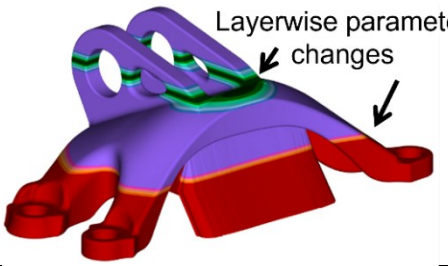	Evaluate process-controlled part against nominal counterpart.
Unsupported, process-controlled GE bracket build	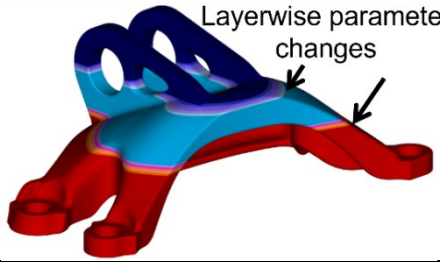	Evaluate process-controlled part against nominal counterpart.

1.5 Broader Impacts and Societal Outcomes

An improved LPBF process is needed in high-value applications where functional performance is unlocked through fabrication of complex geometries with advanced material properties infeasibly produced with other manufacturing techniques. As shown in Figure 1-4, an advanced, model-guided process control approach ultimately enables significantly improved part quality as compared to standard, constant parameter strategies.

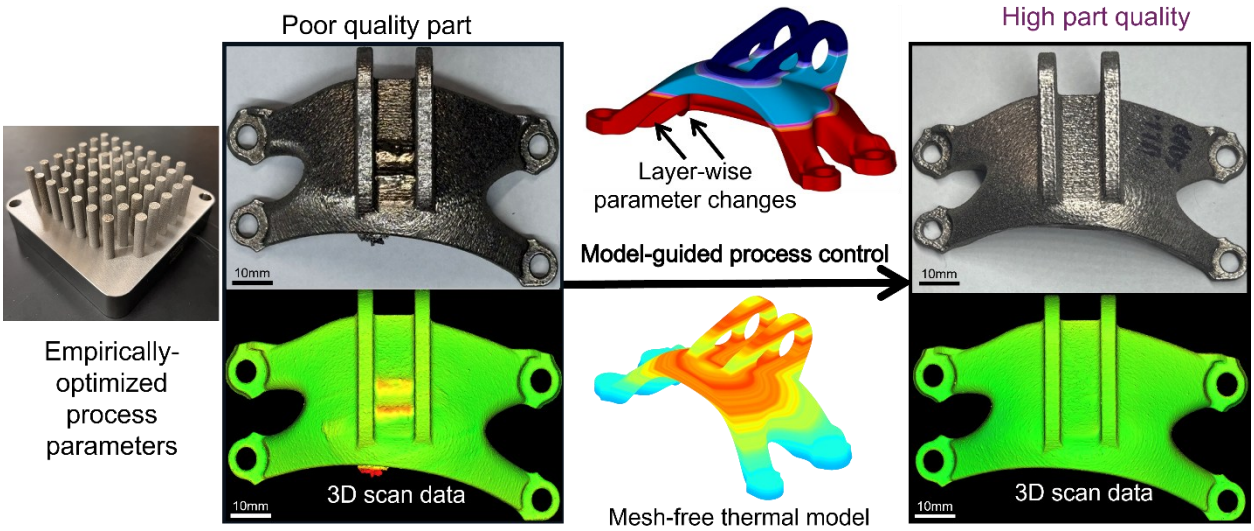

Figure 1-4: Benefits and necessity of process control.

Key to the aerospace industry, LPBF has enabled improvements in propulsion design, testing and manufacturing, critical to furthering our society's need for commercial flight, space exploration, satellite, and GPS technology. It cannot be overstated how important satellite and space research is to human life: agriculture, communications, education, and medicine all benefit greatly from this technology [50]. Focusing on propulsion applications, leveraging the geometric freedom enabled by LPBF, several flow manifold design strategies are shown in Figure 1-5, such as single channel, multi channel, and complex cavity approaches. Each of these strategies offer benefits by promoting heat transfer, fluid mixing, and flow characteristics locally.

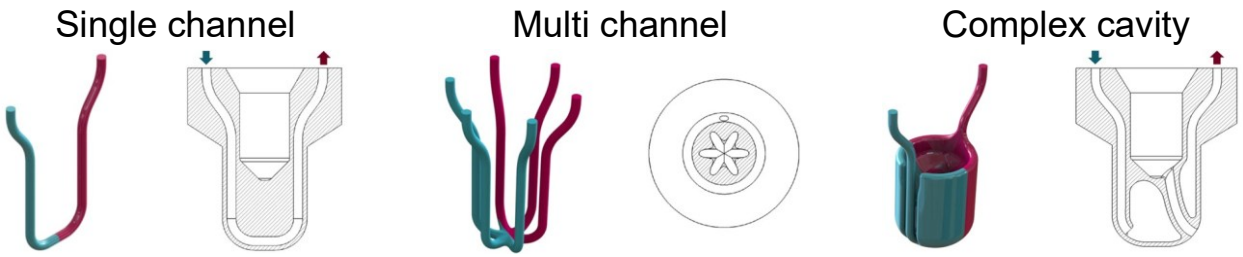

Figure 1-5: Examples of conformal cooling strategies for propulsion applications [51].

For liquid propulsion applications, the injector component, which determines how a fuel and oxidizer are mixed, is highly influential on overall thrust performance and efficiency [52]. As shown in Figure 1-6, two injectors are shown during water flow testing. In Figure 1-6(a), a Nanolaunch (cube satellite) program injector was fabricated in Inconel 625 (IN625) using liquid Oxygen (LOX) and Propane propellants. In Figure 1-6(b), an Additive Manufacturing Demonstrator Engine (AMDE) injector was fabricated in IN625 using LOX and gaseous Hydrogen (GH2) propellants. While there still exist challenges such as feature resolution and surface roughness, further LPBF advancements make AM-forward injectors an increasingly viable choice for next-generation rocket engine components owing to their part consolidation and design freedom of manifolds.

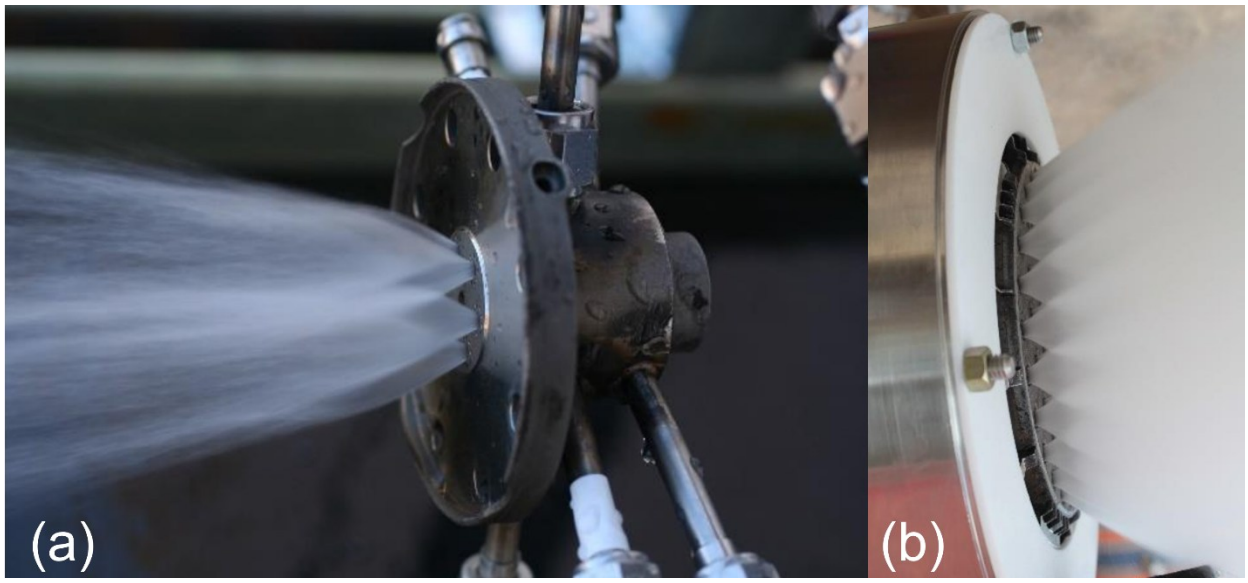

Figure 1-6: Two examples of NASA's LPBF bipropellant rocket injectors [53].

There exist active research questions to advance LPBF improvements, spanning improved process reliability [54], reduced process variability [55], and strict regulation of the process while maintaining part quality. Through a process control approach, strict regulation of the LPBF process through advanced process control can minimize defects such as porosity, distortion, and build failures. This approach not only enables improved part quality, but also increases productivity through faster build rates, accelerated part-parameter development, and quicker time to market of certified components.

Ultimately, LPBF shows promise to better compliment traditional metal manufacturing processes where functionalities and cost savings are sufficiently gained. As such, cost savings could be achieved at various stages of the process with advanced process control implementation. Pre-qualification, the costs of print parameter studies and development could be vastly reduced by circumventing traditional, expensive and cumbersome experiments. During the printing process, lower material waste and machine run costs could be achieved by reducing build failure rates, while maximizing productivity, a major disadvantage of LPBF [56]. In the post-processing and part qualification processes, a more adaptive process reduces the need for supports, therefore lowering the costs of expensive support removal and part-machining. Eventually, the summative gains at each of these process steps could lead to accelerated part qualification, resulting in digitally- and physics- verified parts at a potential of millions of dollars saved throughout the part qualification process [39].

2 Literature Review

This chapter reviews prior work in process control strategies in LPBF while highlighting the challenges and advantages of each approach, with the goal of identifying gaps addressed in this thesis. Within this scope, process control can be categorized into either model-based feedforward control or sensor-based feedback control approaches. Further, the application governs the next subset of categorization, where control techniques can be applied to the meltpool (i.e. trackwise), layerwise features (i.e. temperature), or other part-specific features. It is noted that while there exist similar choices of control (trackwise, layerwise), the design space for implementation of control strategies could change greatly: over 100 independently controlled process parameters could be modified for process control in LPBF [57].

2.1 Feedback Control

In feedback control applications, real-time sensor data is used to inform a controller that adjusts process parameters to minimize error from a target output. For example, if an IR camera detects higher meltpool temperatures than targeted, the controller can reduce energy input to converge on the desired target meltpool temperature value. A key benefit of feedback control is its adaptability: it leverages real-time measurements to correct process drifts as they occur. While feedback controllers can determine appropriate parameter adjustments, implementing these changes parameter choice is often limited to lack of access to process variables on commercial machines. As a result, open-source machines are preferred for developing and testing such control strategies.

Table 2-1: Examples of feedback process control approaches in LPBF.

Ref.	Motivation	Control Method	Conclusion
Shkoruta et al. [58]	Meltpool greatly affects part quality; feedback control is difficult due to its small spatial and temporal scales.	Meltpool intensity control by modulating laser power using a feedback controller and a coaxial, near-infrared (NIR) camera sensor.	Meltpool intensity errors were reduced by up to 50% when compared to open loop conditions.
Vasileska et al. [36]	Overhang features cause overheating, resulting in geometric inaccuracy.	Meltpool laser heated area (LHA) control by changing the laser duty cycle and scan path length.	Improved surface flatness and mean error by 67% for an overhang geometry compared to nominal.
Park et al. [59]	Stable meltpool properties are required to produce high quality parts.	Meltpool size index control by modulating laser power using a reinforcement learning (RL) model.	Improved meltpool intensity variation by up to 62% and reduced experimental error by up to 49%.
Kavas et al. [32]	Variation in surface temperature is associated with process errors and defects.	Layerwise surface temperature control by modulating laser power using closed-loop IR camera measurements.	For initial layers, 2% error of target temperature is achieved. Eventually, low power input generates porosity, leaving stable process regime.
Rezaeifar et al. [60]	Different porosity mechanisms deteriorate part quality.	Layerwise meltpool temperature control by modulating power using closed-loop IR camera measurements.	Despite high or low temperature perturbation, the controller converged to the defect-free zone in approximately 10-20 layers.

Shkoruta *et al.* [58] implemented a feedback control method applied to trackwise meltpool intensity control through intralayer laser power changes. With their controller design, both feedforward and feedback control modalities are enabled, but focus on the feedback implementation for bare metal tracks without powder, as a baseline, and on built-up tracks to tune their controller. Finally, when applied to experimental cube geometries, meltpool intensity errors were reduced by over 50%.

Leveraging in-situ monitoring, Vasileska *et al.* [36] used feedback control to regulate an observed laser heated area (LHA) by varying the laser duty cycle and scan vector length. First, the controller was calibrated on simple test geometries and then applied to a 5 mm bridge overhang specimen, achieving 67% reduction in surface flatness and mean error as compared to the nominally-printed baseline. Notably, with their open-architecture software, controlling laser duty cycle is claimed to be more effective than power control, beam shaping, and velocity control, owing to its fast control. Additionally, this method performed well on a bridge overhang, demonstrating effectiveness in low conductivity part regions.

Using a reinforcement learning (RL) approach, Park *et al*. [59] developed a framework to first construct a data-driven spatiotemporal model of the meltpool size index, train their RL model, then deploy their learned control strategy in physical experimentation. In this approach, for a suite of 10 geometries, meltpool signal variation was reduced by 42-62% and experimental error reduced by 30-49%. Additionally, it is noted that while the RL error and variation reduction showed insignificant performance over a comparable feedforward and feedback approach (30% and 36%, for the RL, versus 32% and 35% for FF + FB), the optimization and development time was greatly reduced from 3,400 seconds to 17 seconds total.

In another work concerning layerwise temperature control, Kavas *et al*. [32] use laser power as the controlling variable and an IR camera for closed-loop control. In prior studies, part-specific temperature targets were obtained for their inverse pyramid geometries, chosen for heat accumulation. Notably, for their overhang geometries, their controller converges to the lower limit of laser power, causing significant LOF porosity, as their model was tuned to a fully-dense part at nominal conditions, not a porous one. Furthermore, this paper demonstrates the importance of

porosity in a controller framework; often times, process parameters are heuristically chosen to deter porosity, but measuring in-situ porosity is difficult.

To combat the issue of porosity, Rezaeifar *et al.* [60] apply a closed-loop, proportional-integral-derivative (PID) controller to control layerwise meltpool temperature by varying laser power. In their experiments, variable meltpool temperature thresholds are first applied to standard density cube samples to show distinct porosity characterization. It can be seen that there exist discrete porosity regimes of keyholing at high apparent meltpool temperatures, a defect-free zone, and lack of penetration (LOP) and LOF porosities at low apparent meltpool temperatures. In a series of experiments, their controller was evaluated by varying the initial laser power purposely low or high, then showing convergence to the defect-free zone after approximately 10-20 layers.

2.2 Feedforward Control

In contrast to feedback control, feedforward control leverages a model's *predicted* output rather than with real-time sensor data. As such, it iteratively simulates a process model to vary process inputs to minimize error between the model's input and a desired target. Once optimized, the model's output parameter plan is then employed experimentally. Notably, this method enables process iteration in a computational environment, saving time and expense associated with extensive physical experiments. However, since feedforward control is performed before the process, it cannot account for process drifts or noise unless explicitly considered in its simulation; feedforward control assumes process disturbances are modelled perfectly.

Table 2-2: Select examples of feedforward process control approaches in LPBF.

Ref.	Motivation	Control Method	Conclusion
Wang et al. [33]	Porosity formation is caused by excessively high or low laser power, especially at laser turnarounds.	Meltpool cross-sectional area control by modulating laser power from an analytic-based, controller simulation.	Increase of meltpool cross-sectional area accuracy by up to 40% and mitigated keyhole porosity formation.
Irwin et al. [61]	Porosity formation is caused by lack of thermal control, leading to incomplete or over melting.	Meltpool volume control by modulating laser power using a secant-based FEA controller simulation.	Reduced meltpool cross-sectional area variation by up to 48.8%
Shkoruta et al. [62]	Meltpool control for LPBF remains difficult due to geometry-dependent behaviors.	Meltpool intensity control by modulating laser power based on an empirically-tuned feedforward controller.	Reduced meltpool intensity error by up to 28% and approximately 50% error reduction in geometry-related variation.
Yeung et al. [63]	Discrete step velocity control in LPBF machines necessitates laser path control.	Meltpool cross-sectional area control by combining jerk-optimized scan paths with laser power changes.	Jerk-optimized paths show higher spatial and temporal accuracy than in conventional implementations.
Yeung et al. [40]	Laser power and scanpath errors can induce material defects.	Meltpool intensity control by modulating laser power based on a geometric conductance factor (GCF).	Improved roughness at downfacing surfaces and decrease in meltpool intensity error.
Ogoke et al. [64]	Meltpool-level defects including porosity and cracking deter LPBF adoption.	Meltpool volume control by modulating laser power or laser velocity numerically using deep reinforcement learning (DRL).	Improved error of meltpool depths by 68.2% and 77.5% for both trajectories, respectively.
Yao et al. [65]	Controlling meltpool-level thermal behavior crucially affects printed layer quality.	Meltpool heat affected angle (HEA) control by numerically changing hatch spacing, laser power, and velocity combinations.	Defects can be categorized into four distinct regimes of heat affected angles and molten layer depths.

Liao-McPherson et al. [66]	Meltpool-level control is difficult at the part scale, so layerwise control enables scalability.	Layerwise meltpool depth and top surface temperature control by numerically modulating laser power.	Root mean squared error (RMSE) as low as 3.37 for meltpool depth and as low as 15.81 for meltpool length.
Druzgalski et al. [39]	Geometrical complexity in LPBF necessitates scalable parameter optimization.	Layerwise temperature control by modulating laser power at defect-probable regions.	Improved surface roughness and geometric accuracy at downfacing surfaces.
Kusano et al. [41]	Lack of literature on the effects of time per layer on layerwise temperature control.	Layerwise surface temperature control by changing time per layer based on FEA simulation.	Microstructural properties of hardness and primary dendritic arm spacing (PDAS) both strongly correlate to target surface temperatures.
Ren et al. [67]	Standard process parameters can lead to overheating at overhang features.	Layerwise temperature control by modulating laser power based on a finite difference model simulation.	Without a lower laser power threshold, reduced variability in meltpool size, reduced meltpool mean half-width by more than 20%, and increased hardness.

With a feedforward control approach, Wang *et al.* [33] demonstrated the feasibility of trackwise meltpool cross-sectional control by power through use of an analytic-based, nonlinear inverse-dynamics controller. In this work, several adjacent track layers were printed, where laser turnarounds and prior tracks can perturb the meltpool's thermal history and resulting porosity; this approach realized a 20-40% accuracy increase of cross-sectional area. In their more recent work, Irwin *et al.* [61] used a secant, FEA-based feedforward approach to regulate the meltpool volume, a key contributor of porosity, through trackwise control of laser power. With this approach, again, several adjacent, alternating tracks were printed, and a 13.4 to 48.8% reduction of meltpool volume variation was realized as compared to its nominally-printed benchmark. Notably, their iterative simulations for the controlled case only took 2.3 times longer than the nominal laser power simulations.

In a different meltpool control approach, Shkoruta *et al.* [62] implemented an empirical feedforward model to control meltpool intensity with trackwise power control. One key finding of this work is that meltpool intensity has an exponential dependence on the length of scan lines, independent of scan pattern orientation or area of their triangle geometries, illustrating how sharp corner geometries thermally disturb a meltpool. Using their power controller, optimized power profiles are obtained for sharp-edged geometries to enable a 14.0% to 28% error reduction in meltpool intensity and approximately 50% reduction in geometry-related variation across test layer scan profiles.

Using an empirical method, Yeung *et al.* [63] propose a geometric conductance factor (GCF) which is based on the relative solid metal to powder ratio, which enables parameter tuning, namely, laser power and velocity. Additionally, jerk-optimized scan paths (i.e. velocity) and laser power are employed to result in higher spatial and temporal accuracy of the laser. Ultimately, the GCF-optimized laser powers combined with constant build speed laser path modes show the most consistent meltpool area measurements. In their later work, Yeung *et al.* [40] leverage their GCF method to improve meltpool intensity through intralayer laser power grading. Critical to meltpool instability, this GCF method is implemented for overhang geometries to generate layerwise laser power profiles. While their determined laser power bounds were relatively conservative, this approach showed improvements of downfacing roughness and layerwise meltpool intensities.

Similarly, Ogoke *et al.* [64] apply a deep reinforcement learning (DRL) framework to numerically control meltpool volume by varying laser power or velocity. Using a simplified 2D model, a meltpool heat distribution is obtained, and YZ, XY, and XZ cross sectional heat distributions are used as the inputs for the DRL model, with rewards based on achieving a target meltpool depth. Comparing the controlled versus the uncontrolled case, 68.2% and 77.5% change

in cumulative, aggregate meltpool deviation errors over all timesteps were achieved for both horizontal and triangular trajectories, respectively.

Using numerical computational fluid dynamics (CFD) modelling, Yao *et al*. [65] simulate multi-track, single layer scans to analyze meltpool behavior. One defining metric of this work is the heat affected angle: the angle between the line connecting the bottom of the first and last molten layers and the horizontal line. So, the larger this heat affected angle, the higher the thermal influence between adjacent layers. Additionally, previously molten layers or tracks greatly affect subsequent scans through preheating. In this work, a back propagation neural network (BPNN) was used to determine the relationship of heat affected angle depths to the process parameters of laser velocity, power and hatch spacing under any combination thereof. Given a trained model, defect categorization can then be grouped into classifications of the heat affected angle and molten layer depth and potentially used for parameter development.

As compared to meltpool control approaches, another common control method in LPBF is through layerwise features or metrics. In a feedforward control approach, Druzgalski *et al.* [39] implement layerwise average temperature control through use of intralayer power changes. A key argument presented in this work is that complex geometries remain difficult to qualify due to feature-specific defects. So, in this approach, feature extraction is first employed to quickly down-select scanpath regions potentially prone to defects, and then a layerwise power plan is chosen from model-validated heuristic laser power choices of 25%, 50% and 75% from nominal. Finally, with these laser power changes, the intralayer power profile is optimized based on overheating detected from a thermal model. With their test geometry, qualitative improvement is clearly shown from a nominally printed part, especially at overhang or bridged features.

Leveraging a high-fidelity 2D thermofluidic simulation approach, Liao-McPherson *et al.* [66] propose a layerwise control architecture to numerically control the meltpool depth and surface temperature by laser power. One important assertion in this work is the relationship between surface temperature and porosity: if the surface temperature is too high or low, which can occur with constant laser power, the meltpool can grow or shrink, leading to defects of cracking, porosity and uneven microstructure. In this work, a multi-layer simulation was conducted to evaluate meltpool predictions across training and validation datasets, with root mean squared error (RMSE) of 3.37 and 3.38 for the meltpool depth respectively, and 15.81 and 15.87 for meltpool length, respectively.

Leveraging feedforward control, Reiff *et al.* [68] designed a controller framework, aiming to combat the inflexibility of most commercial LPBF systems. First, an experiment was conducted to establish the process map relationships of laser power, velocity, and surface temperature with a radial basis function (RBF) network. Applying their controller framework, aimed to improve uneven temperatures in corners, their results show a simulated 48% improvement in temperature standard deviation.

Kusano *et al*. [41] used dwell time, or time per layer (TPL) to control layerwise surface temperature using an FEA-based feedforward controller. In this work, a quarter-scale FEA model is used for a radially-symmetric part geometry designed to restrict heat transfer to the substrate. Further, within vertically sectioned regions of the part, different target surface temperatures were chosen to validate TPL-temperature control and found that both primary dendritic arm spacing (PDAS) and hardness both correlate significantly to the target temperature, illustrating a method to obtain graded microstructure in the LPBF process.

Recently, Ren *et al.* [67] used a feedforward modelling approach to control layerwise temperature by optimizing laser power. Using a target threshold for interlayer power, a feedforward model then adaptively outputs layerwise laser powers once overheating is detected. For experimental comparison, three groups of parts are constructed: an optimization scheme without a laser power bound, one with a lower power bound, and baseline specimen. Notably, without a laser power constraint, the interlayer temperature stabilized on its target but generated significant LOF porosity. With a lower bound specified, convergence on this target was not met, but did show more than 20% improvement in meltpool half-width and increases in microhardness. Interestingly, convergence on a porosity-acceptable laser power shows promise to produce a higher quality part through a more consistent meltpool and microhardness, but convergence on an aggressive temperature target may not be possible with layerwise power changes.

3 Experimental Setup

3.1 LPBF System

All bracket geometries were manufactured on an SLM 280 2.0 LPBF system equipped with a 400W single laser. The gas-atomized Truform 718 (IN718) powder feedstock was sourced from Linde. Each reduced-size build plate used was approximately 100 mm x 100 mm by 30 mm. A Micro Epsilon TIM 640 long wave Infrared (IR) camera installed within the LPBF machine was used to obtain top surface temperatures of each build during the printing process.

Table 3-1: Specifications of the TIM 640 IR camera used.

Spectral range [µm]	8-14
Frame rate [Hz]	33
Image resolution [Pixels x pixels]	640 x 480
Spatial resolution [Pixels/mm^2]	10

Calibration of the IR camera to absolute temperatures was performed and is explained in our prior works [4, 37] and in Chapter 4. Prior to each build, the build atmosphere was purged with argon to maintain a maximum of 0.2% oxygen during the print process.

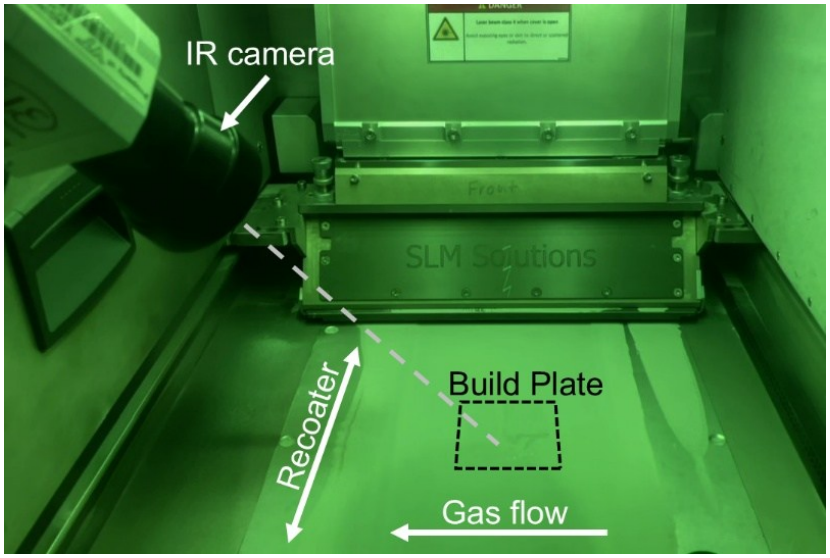

Figure 3-1: SLM 280 2.0 build chamber with IR camera, recoater and gas flow directions.

3.2 Experiment Design

3.2.1 Process Parameters

The process parameters used for this work are summarized in Table 3-2 below. All of the following process parameters were used for each bracket build, except for the hatch laser power and velocity, which were modified layerwise for process-controlled builds. Based on the results from the porosity DOE, 210 W and 880 mm/s were selected to allow for a wider range of PV adjustments in subsequent process control simulations and build preparation implementation.

Table 3-2: Modified SLM 280 1N718 process parameters for uncontrolled bracket builds.

Nominal Process Parameters, [Units]	Values
Layer thickness [mm]	0.03
Hatch spacing [mm]	0.09
Hatch power [W]	210
Hatch velocity [mm/s]	880
Contour power [W]	150
Contour velocity [mm/s]	450
Downskin power [W]	210
Downskin velocity [mm/s]	880
Laser spot size [mm]	0.068
Scanning strategy	Stripe rotation strategy with 67-degree rotation between layers.
Substrate preheat temperature [°C]	100
Recoater cycle time [s]	10 ± 2 (variation due to machine limitation)
Build atmosphere	Argon
Gas flow speed [m/s]	24
Chamber gas pressure (mbar)	12

3.2.2 Porosity DOE

The goal of this experiment is to determine acceptable power-velocity (PV) parameters specific to IN718 for the SLM 280 2.0. For this study, an acceptable power-velocity set is defined as one with greater than or equal to 99.5% density and one without any pores greater or equal to 30μm in its max dimension. Given SLM's suggested parameters, shown in Table 3-2, power and velocity were varied at nominal hatch spacing. A 6x6, full factorial DOE was selected: ranges of

velocity [600, 1300] mm/s and power [150 300] W were chosen to ensure that all regions of a typical porosity-P-V relationship were visible: lack of fusion (LOF) porosity at high velocity/low power, low (<0.1%) porosity at nominal conditions, keyhole porosity at high power/low velocity, and potentially balling, at high power/high velocity [69], as shown in Figure 3-2. Parameters in the lower left of this PV diagram (low power, low velocity) are excluded from the down-selected PVs as they are unproductive; parameters in the top right (high power, high velocity) are also not used for this work as they incur meltpool instability. Porosity is chosen as the determining metric for PV combinations due to its strong influence on mechanical properties, such as tensile strength and fatigue strength variability [70].

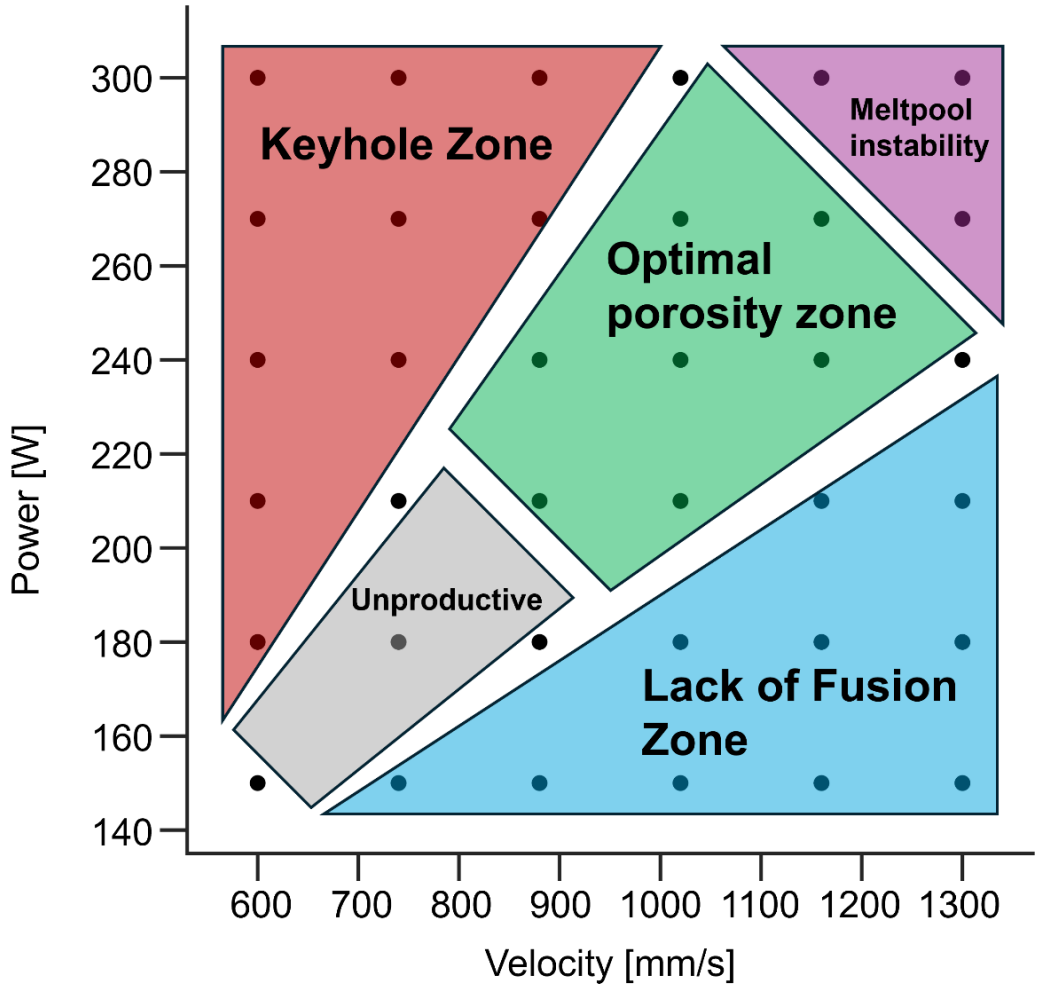

Figure 3-2: Porosity DOE parameter space overlaid with LPBF-typical porosity regimes.

As shown in Figure 3-3, each sample is a 5 mm diameter, 25 mm tall cylinder. Note that only 36 of the 54 total samples shown are pertinent to this work. Additionally, the applied parameter sets were randomized to minimize the influence of uncontrolled variables.

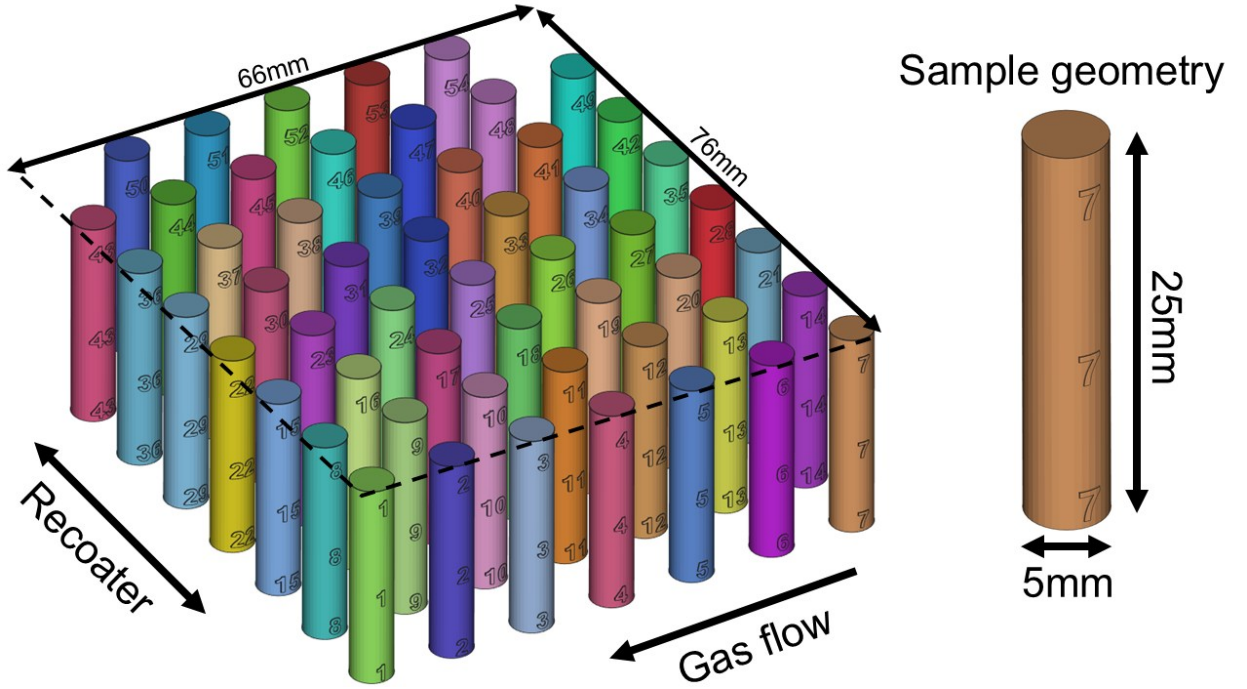

Figure 3-3: Porosity DOE build plan outline with sample geometry.

To characterize these samples' porosity, the top 20 mm of all samples were first cut off using Electrical Discharge Machining (EDM); these upper sample portions were reserved for research not pertinent to this work. The remaining 5 mm of all 54 samples connected to the build plate were polished to prepare a surface for microscope analysis. All samples were simultaneously polished on a Buehler Automet 300 polishing machine while connected to the original build plate. These samples were polished with 300 to 1200 grit size, then with 6 µm and 1 µm diamond suspension and 0.05 µm colloidal silica for 4 – 5 minutes at each grit size. The as-printed build and post-processed build plate with EDM-cut and polished samples is shown in Figure 3-4.

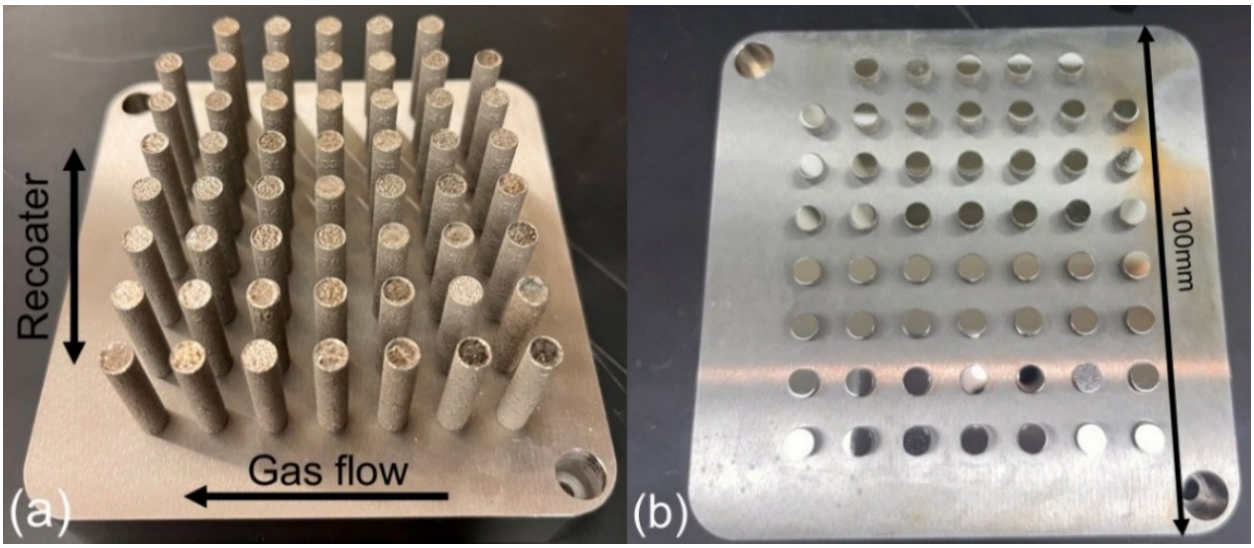

Figure 3-4: Porosity DOE build. (a) As-printed samples. (b) EDM-cut and polished samples.

Once polished, each of the 36 samples' top surfaces was microscope imaged on an AmScope BH200-MR microscope equipped with an AmScope MU Series 10.0MP C-Mount camera with a resolution of 2.93 pixels/μm [71]. Approximately 30 images were taken at each sample's surface at 10X magnification to capture the entire exposed surface. Each sample's respective images were processed in MATLAB scripts to highlight valid pores and to define exclusion regions: polishing or drying artifacts and regions outside the circular part boundary. Within each non-exclusion image, porosity is determined from the image pixels where percentage porosity $= 100\%$ x $\frac{\text{valid pore pixels}}{\text{total valid pixels}}$. A sample workflow is shown in Figure 3-5.

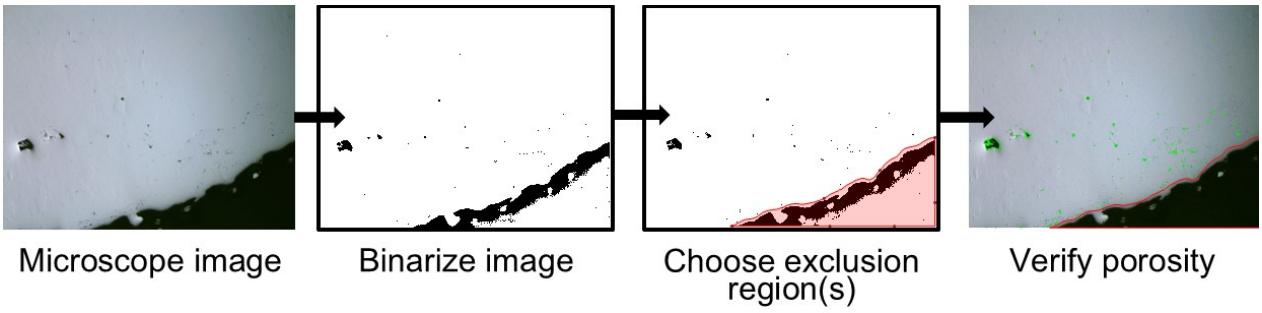

Figure 3-5: Microscope image porosity data workflow.

While CT scanning of these specimens would be most ideal to fully capture porosity locations and severity, due to lack of machine availability, a microscope image and analysis was

chosen instead. Notably, only the top face of the remaining 5 mm of each sample was analyzed, therefore restricting potential sample to a single layer rather than for the entire part. A key tradeoff is noted in this geometry choice: while a small cross-sectional area accelerates microscope image capture time, it also prints less tracks per layer, lessening overall sample count of meltpool tracks, and therefore making the results more prone to variation than for a larger, higher-area specimen. Lastly, it is noted that the sample geometry is one with a constant cross-sectional area, analogous to standard porosity test coupons. By printing the same geometry with a constant cross-section, variation due to thermal history effects are minimized. However, a key assumption underlying this approach is that process parameter-porosity relationships can be generalized to different, more complex geometries – an assumption widely regarded in literature as weak [70], [72], [32].

3.2.3 Support Strategy Design

To evaluate process control effects and part quality metrics across a spectrum of supporting strategies, two distinct support strategies were designed for this geometry named the partially supported and the fully supported brackets. In terms of geometry, these support strategies are designed to primarily support the two overhang features noted in Figure 3-6, the thin wall overhang feature, or “front lip”, and the large overhang feature, or “underbelly”. Using these geometrical primitives, the fully supported strategy fully attaches to these features at flat faces and where the overhang angle is less than or equal to 45 degrees. Comparatively, the partially supported strategy reduces support volume by 45% by reducing the thickness and connection location of the underbelly and front lip features with a minimum 35-degree overhang angle. As shown in Figure 3-6, the three support strategies illustrate the connection locations, thickness, and overhang angle with bottom-up and cross-sectional views. Notably, in the cross-sectional views, directly behind

the front lip feature, a small overhang is unsupported, with the expectation that this region creates overheating, and therefore results in distinct thermal histories.

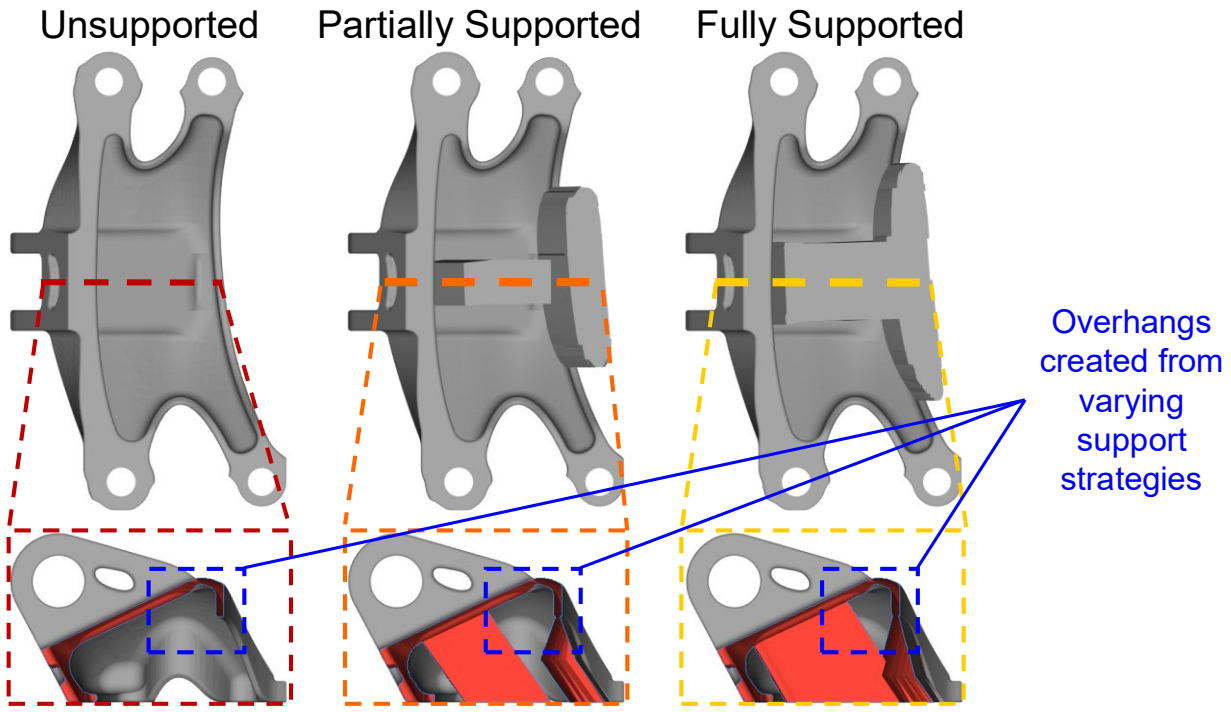

Figure 3-6: Bottom-up and cross-sectional views for the support strategies.

It can be seen that the support volumes are fully dense, and the part-support connection interface is non-sparse with uniform attachment; this is due to limited graph theory model fidelity of thin-walled features. In terms of process parameters, the support process parameters do not differ from the part's due to current inability to generate intralayer parameter changes in both the build file development software and model interlayer parameter changes in the current graph theory model. Notably, these geometry and process parameters differ from industry-typical support strategies, where supports are typically sparser, and printed with lower energy input process parameters to promote removability. A major consideration of practical support design in LPBF is ease of removal: a key tradeoff is that while denser supports maintain part dimensionality through mechanical support and thermal dissipation, they become increasingly difficult to remove either

manually or with machining [73]. In this work, support removal is deemed less important than their effects on thermal history and resulting part quality, so these supports are instead machined.

3.2.4 Bracket Build Overview

To evaluate the effects of process control on part quality for this topology-optimized aerospace bracket, process control and lack of process control was varied across three supports levels: unsupported, partially supported, and fully supported, as depicted in Figure 3-7

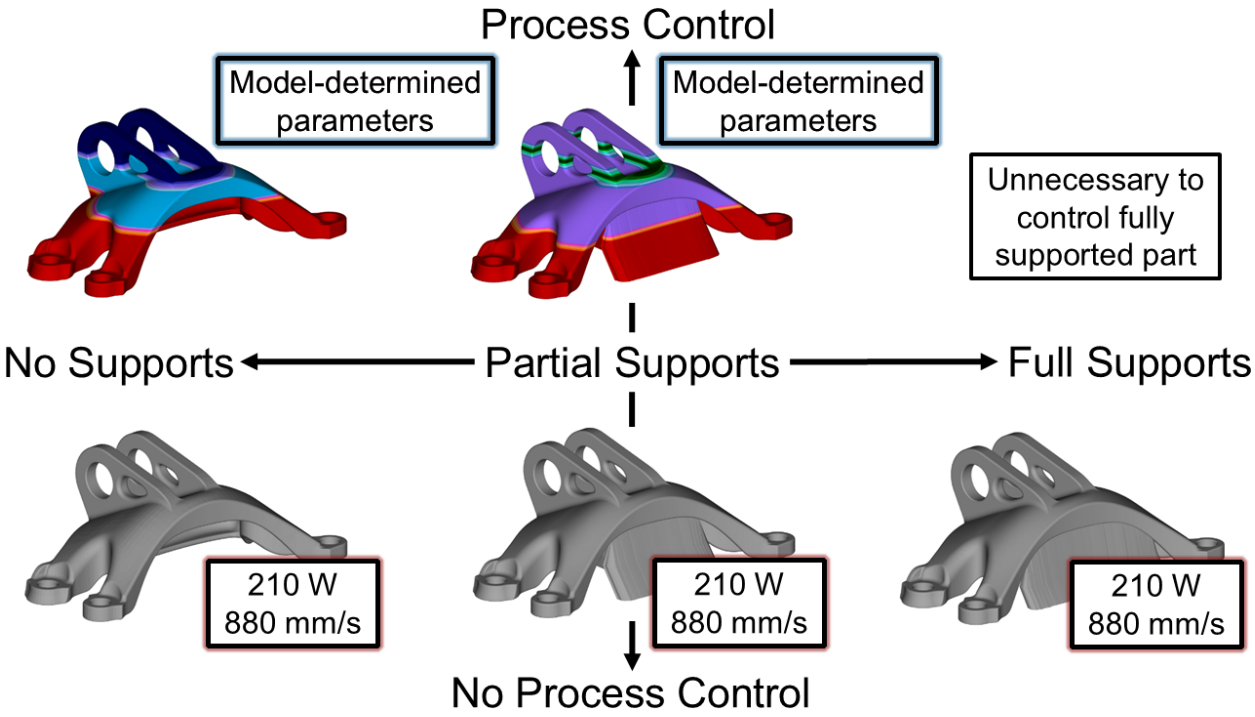

Figure 3-7: Build plan for the brackets across support profiles and process control conditions.

The five bracket builds follow a consistent build plan layout: each bracket was centered on the build plate with a 15-degree clockwise rotation to reduce the effects of recoater-part collisions and promote powder spreadability [74]. With the same baseline geometry, these builds are categorized by differing support strategies (fully, partially, and unsupported) and whether process control was applied. For controlled builds, the hatch PVs were determined from a feedforward

graph theory simulation to emulate the target temperature profile of the fully supported geometry. The simulation methodology for deriving the process-controlled hatch PV settings is outlined in chapter 4.

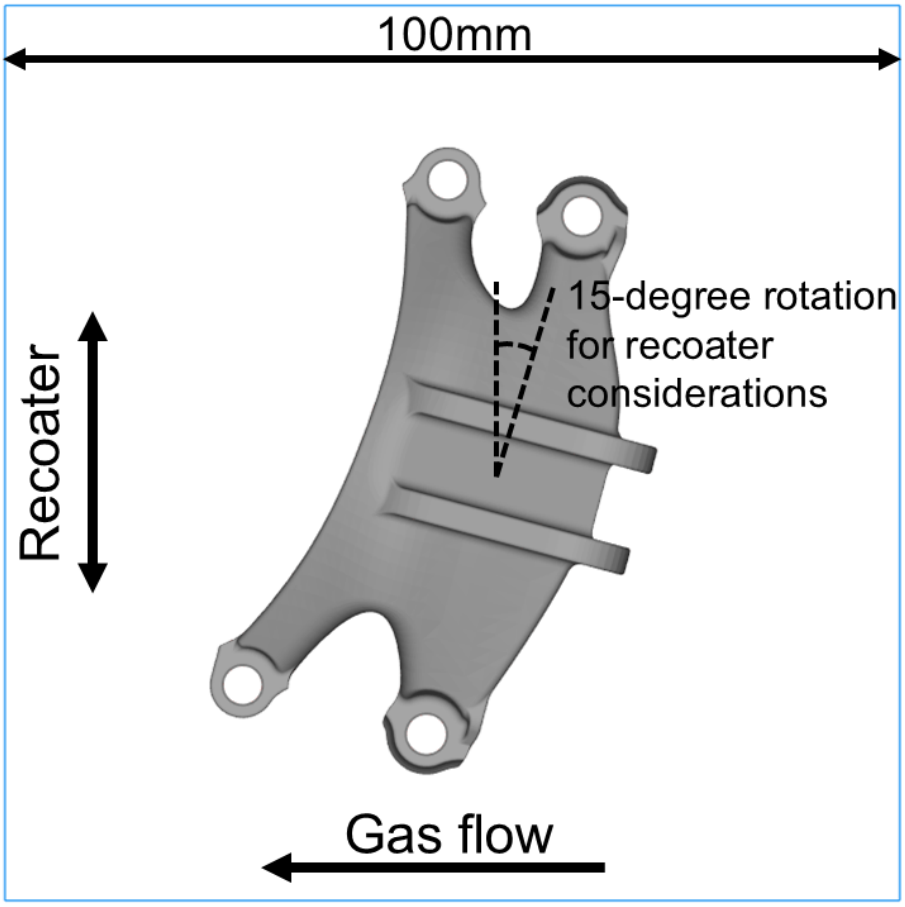

Figure 3-8: Representative build layout for each bracket build.

Each build was fabricated on the same SLM 280 2.0 LPBF system using identical environmental conditions and process parameters, excluding hatch PVs for controlled builds, to ensure experimental consistency. After printing, each bracket was removed from the build plate using EDM. Additional machining was required to remove the supporting structures for the partially supported and fully supported brackets to promote inspection of the underbelly features.

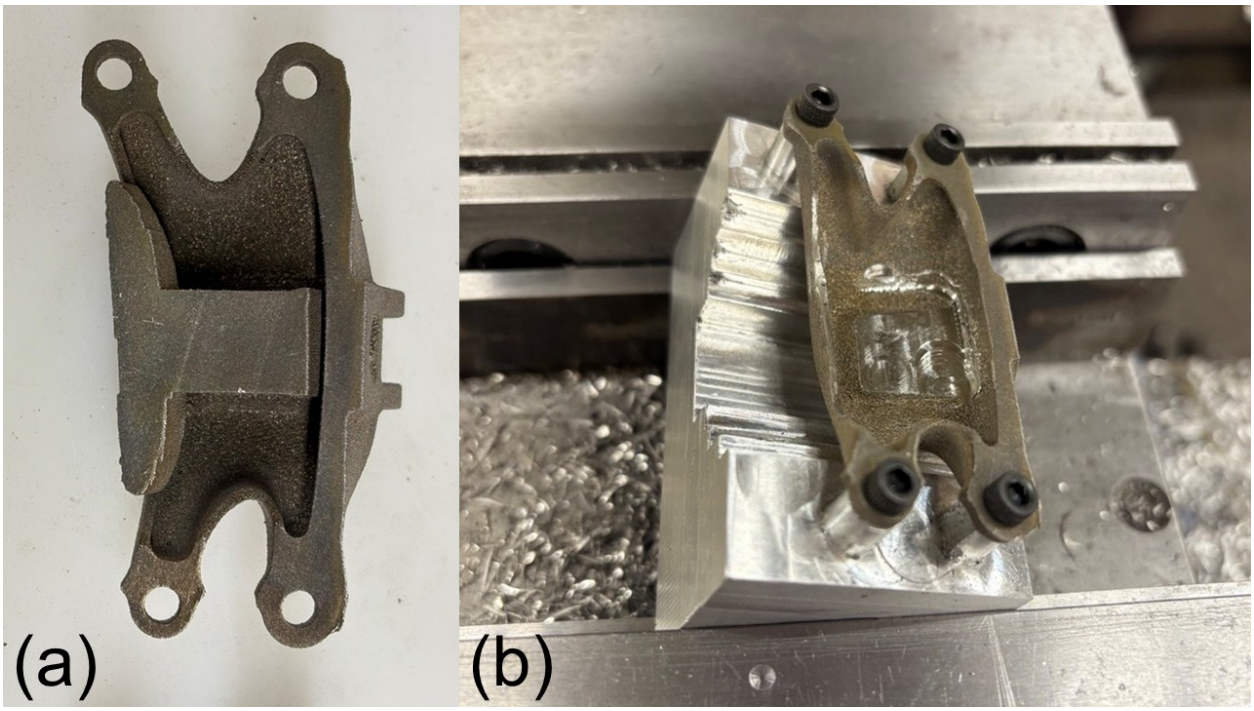

Figure 3-9: (a) Fully supported bracket after EDM removal. (b) Fully supported bracket with custom tooling and supports machined.

3.3 3D Scan Measurement

Upon support removal, if necessary, each bracket was 3D-scanned on an Artec Micro scanner with a resolution of 29µm and accuracy of 10µm [75] to assess geometric deviation of each part as compared to its as-designed target geometry. Artec Studio software was used to autonomously reorient and capture point cloud data of the bracket once mounted. Once the bracket was finished scanning, as determined by the Artec Studio software and upon human verification, the 3D point cloud was post-processed to remove scan points not connected to the bracket. The post-processed 3D point cloud is then imported into CloudCompare software [76], aligned with a target geometry in an STL file format, and a signed-distance map is generated to quantitatively measure geometric deviation.

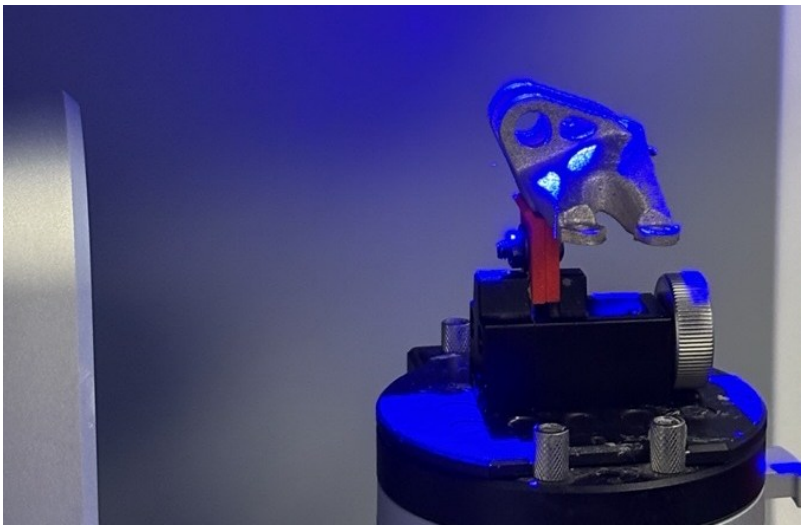

Figure 3-10: As-printed bracket during 3D scanning.

To align the 3D-scanned STL to the target geometry STL, a manual, feature-based adjustment method was used, as automatic alignment incurred excessive error. As shown in Figure 3-11, sample alignment features were used to fully constrain the scanned geometry to the target geometry in the X, Y, and Z, planes. For example, in the XY plane, the four outward pin connection holes were used to constrain rotation with respect to the Z-axis, whereas the parallel pin connection features were used to constrain translation in the X and Y directions.

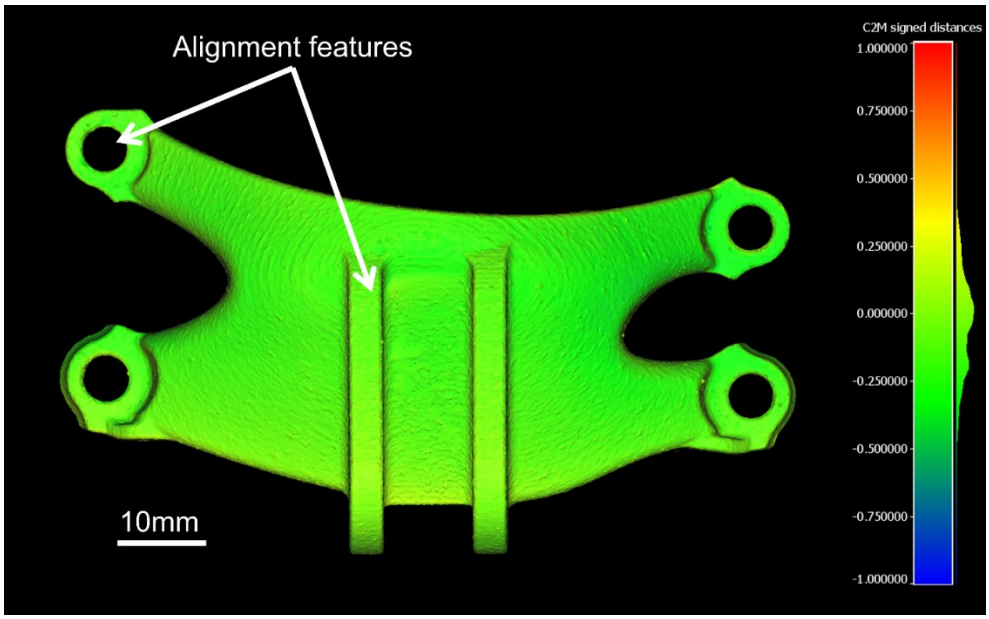

Figure 3-11: Alignment features for comparing as-scanned geometry to target geometry.

4 Process Modelling and Control

4.1 Graph Theory Thermal Modelling

4.1.1 Process Dynamics, Assumptions, and Limitations

The graph theory-based thermal model employed in this work relies on a connected graph of nodes, rather than a traditional finite element (FE)-based method comprised of 2D elements or 3D element voxels. As shown in Figure 4-1, similar to other LPBF simulation tools, heat is applied and activated layerwise, commonly referred to as element birthing. Additionally, a superlayer, or lumped-layer approach simulates multiple layers at once, reducing computational expense.

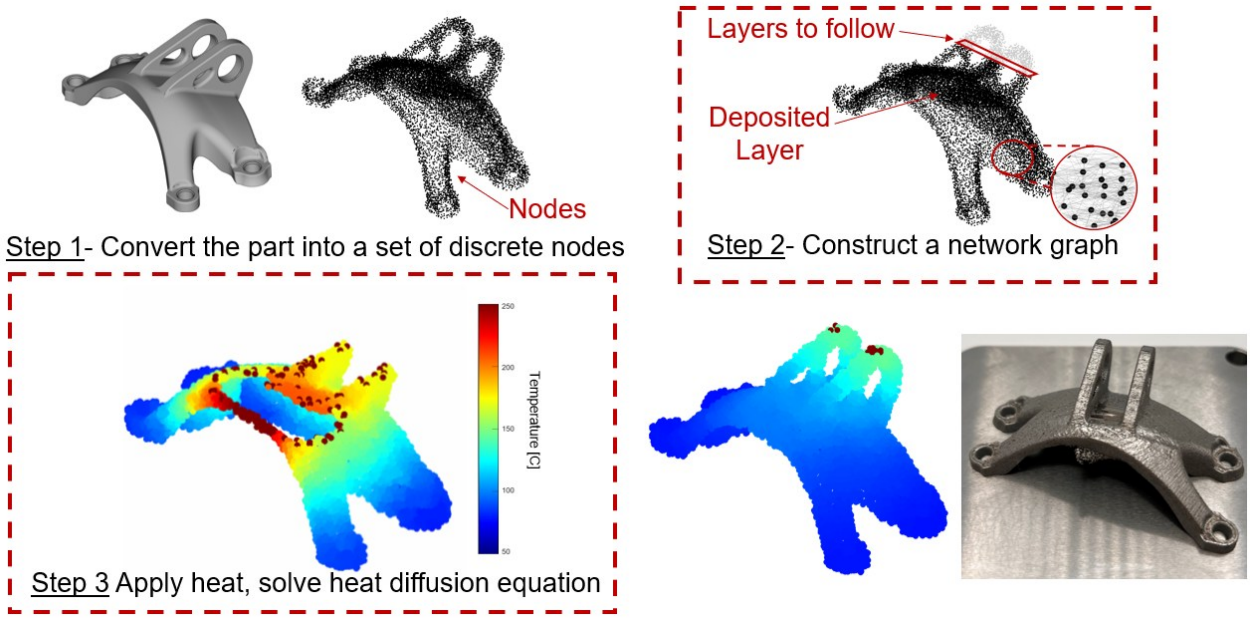

Figure 4-1: Overview of graph theory thermal simulation approach. Adopted from [77].

At a typical layer within this time-dependent heat diffusion problem, the primary initial condition is the top superlayer's temperature equal to the liquid temperature immediately at its activated timestep. Further, at this superlayer, there is heat loss to convection at the topmost surface, heat loss to the surrounding powder, and heat conductance through the part to the substrate. As further superlayers are activated, or printed, the previous layers also heat to melting, which affects defect formation mechanisms and influences material microstructure [78].

A key limitation of this model is the lack of a mechanical (strain-based) component which inhibits distortion or residual stress modelling, which is necessary in unsupported regions to improve print fidelity. As opposed to coupled thermal-mechanical finite element analysis (FEA) approaches [79] or mechanical-only inherent strain approaches [80], this model only simulates LPBF heat diffusion to compute a temperature distribution as a function of space and time as each node superlayer is activated.

Another missing element in this model is meltpool- or hatch-level simulations that could be useful for modelling meltpool characteristics and potentially porosity. As opposed to time-dependent and scanpath-dependent meltpool simulation, this approach activates the superlayer at the material's liquid temperature instantaneously. While hatch-level meltpool simulation is useful for correlating to microstructure [81], geometric accuracy [81], porosity [60], and thermal gradients [82], its simulations require a high computation burden, often taking days to weeks to simulate a full part's scanpath [83].

At the time of writing, a current model limitation lies in assuming constant-temperature material properties as opposed to temperature-dependent material properties, which would theoretically improve model accuracy, all else equal. A key tradeoff is listed in this choice: temperature-dependent material properties require reformulation of the Laplacian matrix which exponentially increases computation time. It is known that important material properties can change significantly for the LPBF process, which include absorptivity [84], thermal conductivity [85], and thermal diffusivity [85]; all of which are model parameters used in this work. As such, future research may involve integrating temperature-dependent properties of this model and evaluating its effects on thermal history prediction accuracy. Additionally, other temperature-dependent properties of the LPBF process not used in this work include modulus of elasticity and

related yield strength [86], hardness [87], emissivity [88], viscosity [82], thermal coefficient of expansion [89].

4.1.2 Simulation Parameters

The simulation process and material properties, specific to the machine-material combination of IN718 and the SLM 280 2.0, are listed in Table 4-1 below. It is noted that the heat loss coefficients listed were obtained and calibrated prior to this work for a similar geometry.

Table 4-1: Graph theory simulation parameters.

Simulation Parameters	Values
Heat loss coefficient part to powder, h_{powder} [W/m^2· °C]	45
Heat loss coefficient part to substrate, h_{cond} [W/m^2· °C]	9000
Heat loss coefficient part to convection, h_{conv} [W/m^2· °C]	42.5
Thermal Conductivity (k) [W/m·°C]	19.47
Density (ρ) [kg/m^3]	8,193
Specific Heat (c_p) [J/Kg·°C]	626
Melting Point (T_0) [°C]	1,609
Ambient chamber temperature, T_{amb} [°C]	77
Node density [Nodes/mm^3]	2.5
Number of nodes	13,408 (unsupported) 18,545 (partial supports) 13,703 (full supports)
Superlayer thickness [mm]	0.12 (4 actual layers)
Gain factor (g) [unitless]	0.6
Computational hardware	Intel i7-13700 CPU, @2.10 GHz with 64 GB RAM.

4.1.3 End-of-Cycle (EOC) Temperature

Prior to printing, each bracket geometry was simulated using a graph theory thermal model to determine its baseline thermal history, exemplified through its end-of-cycle (EOC) temperature: the effective average temperature of each layer immediately before laser strike.

Now, to evaluate process control effects on these geometries, a process control target needs to be first determined. In this work, a constant temperature target was chosen as the control target,

as a stable part temperature is desired to homogenize microstructure and properties – more so than in an uncontrolled instance [41]. It is noted that while EOC temperatures have corresponded to more homogenous microstructural properties, the choices of a spatial average and end-of-cycle temporal definition reduce resolution of the thermal history and therefore resolution of its potential applications: spatially through averaging which circumvents region analyses and temporally which circumvents meltpool-level thermal history contributions. For example, if one wanted to achieve a controlled or as-designed microstructure, the cooling rate of the part must be directly controlled [90]. Moreover, to control defects associated with warpage, one must control meltpool characteristics, especially as local heat transfer boundary conditions change with respect to part geometry [36]

Key to this approach is the recreation of a thermal history of the fully supported bracket: to build a less supported part well, its thermal history should emulate that of a supported bracket to maintain a stable manufacturing process. So, the fully supported bracket was first simulated, then, to emulate the target thermal history at the critical overhang feature, a target constant temperature target was heuristically set at 110 °C, as shown in Figure 4-2. It is noted that the target temperature is lower than the majority of the EOC result; this value is chosen as a conservative lower bound to add additional overshoot to the process control algorithm and test controller responsiveness to this perturbation.

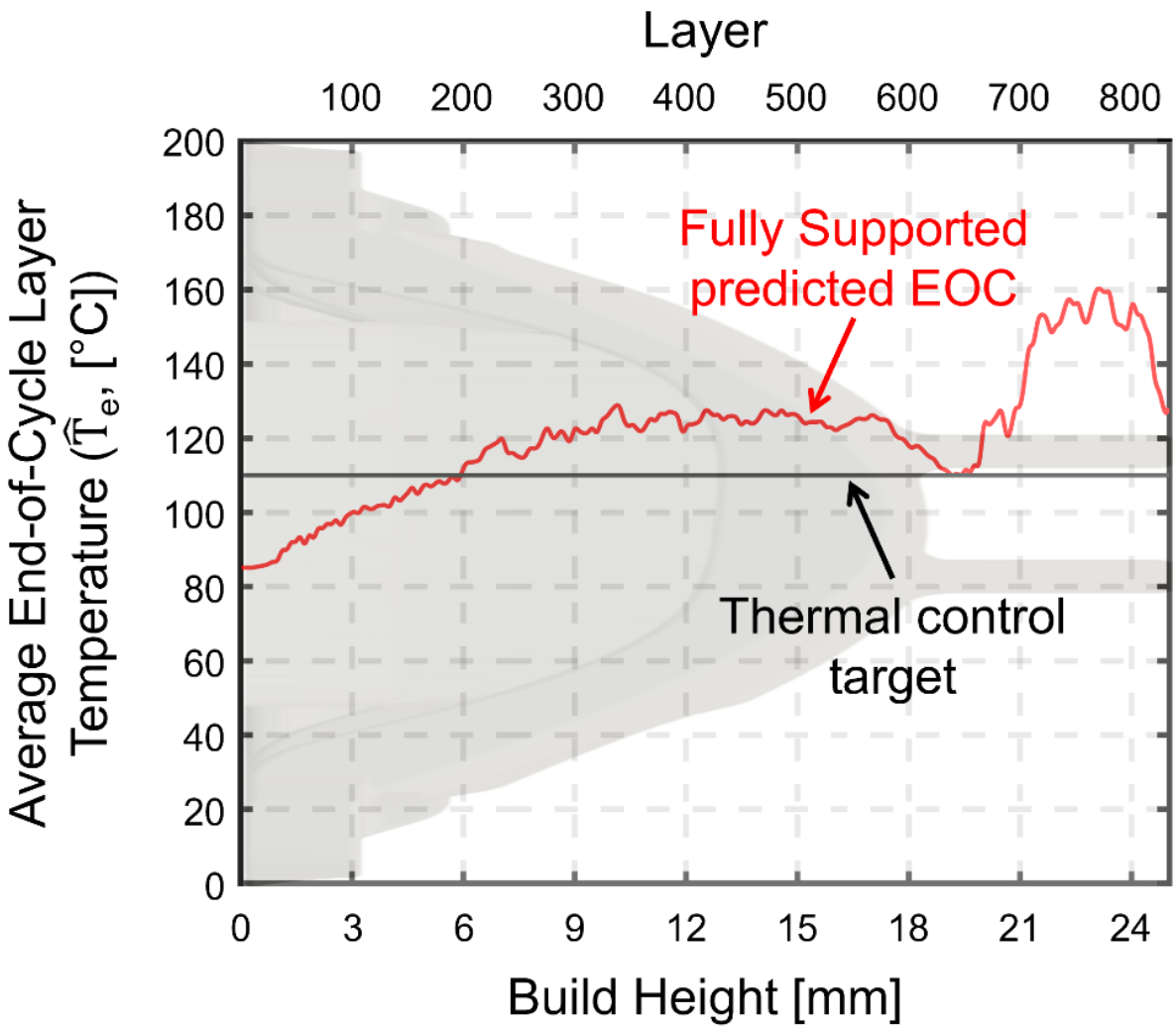

Figure 4-2: Fully supported bracket's EOC temperature and thermal history control target.

4.2 Model Validation

4.2.1 IR Temperature Calibration

The thermoIMAGE TIM 640 IR camera captures relative temperatures, so calibration to a known temperature is necessary to achieve accurate in-situ images of the part. Additionally, calibration of the IR camera to a ground truth temperature is necessary due to setup-specific changes in the IR camera, such as location and angle of the mounted camera, if any other IR camera software parameter changes are made, and emissivity of the surrounding power or solid metal build plate [37]. Figure 4-3 shows the experimental setup required to heat an IN718 cube with powder to a known temperature as measured with a thermocouple. Notably, this method is specific to the material used in this work (IN718) because the emissivity and subsequent temperatures are material-dependent [91]; if the printed material was changed, the IR calibration would be void.

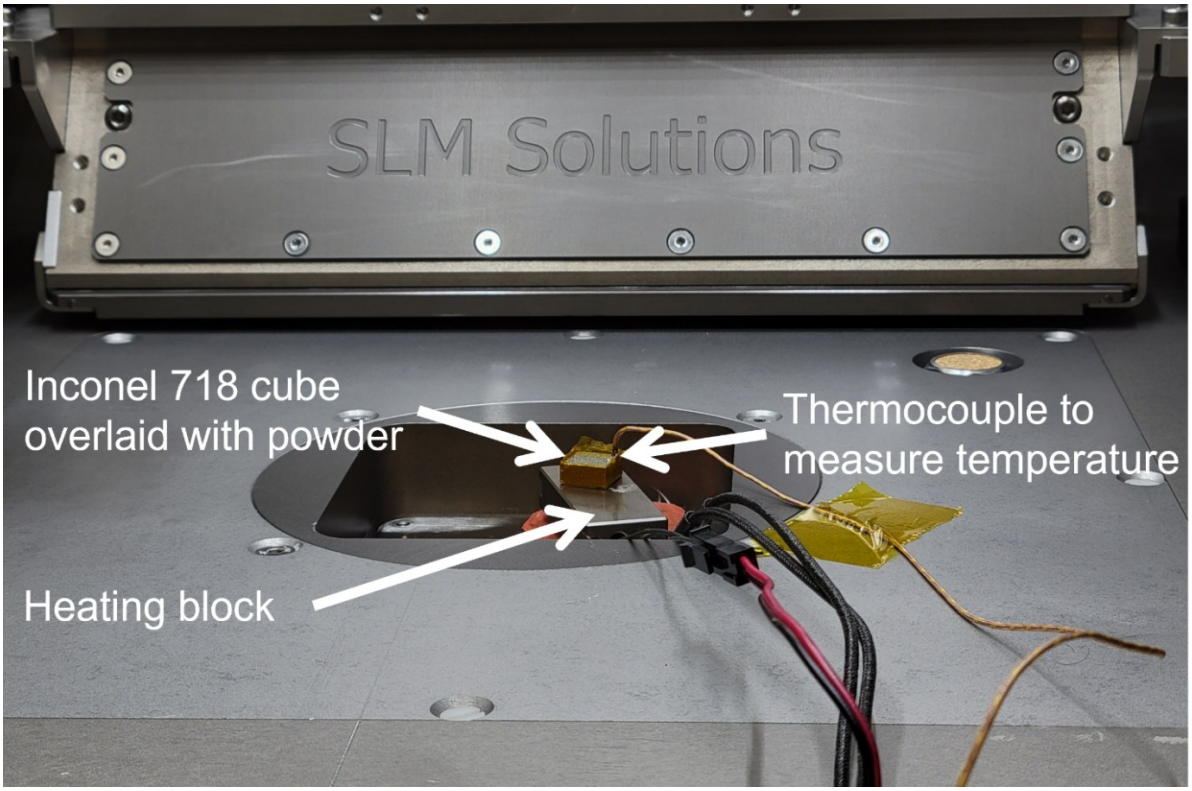

Figure 4-3: Setup of IR camera calibration of a heated IN718 cube to a known, thermocouple-measured temperature.

The temperature of the IN718 cube was raised to temperatures between 25 °C and 325 °C, which covers the range of EOC temperatures for IR temperature processing. Shown in Figure 4-4, the IR temperatures are calibrated to the thermocouple-measured temperatures, achieving an R^2 value of 0.9997 and a root mean squared error (RMSE) of 1.519 °C. Further, to convert a raw IR footage to real-world, calibrated temperatures, two separate temperatures are required. First, the raw IR video (.YUV file format) is converted to its corresponding temperature in the Micro-Epsilon's TIM Connect software, then the temperature is converted to real temperature based on the calibration. The .YUV file to TIM Connect temperature conversion must be performed for each build, but the TIM Connect to real temperature conversion can be performed and reused multiple times, provided no IR camera movement or image parameters are changed. The function used in this work was MATLAB's *poly2* function within its curve fitting toolbox [92].

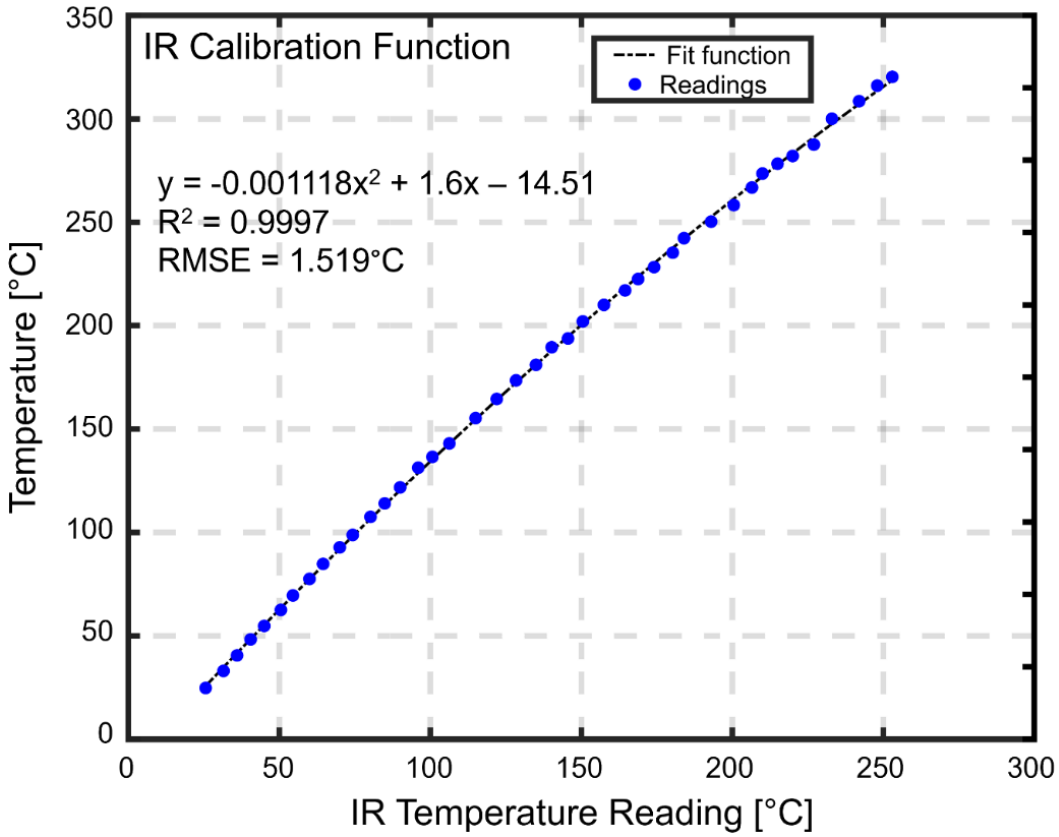

Figure 4-4: Calibration curve for the long-wave IR (LWIR) camera on the SLM 280 2.0 system.

4.2.2 IR Image Processing

Once calibrated temperatures are obtained, further processing is required to compute the EOC temperatures for which graph theory's EOC temperatures can be compared to the model. For each layer, human-verified EOC temperatures are selected to serve as that layer's representative temperature with respect to that layer's temperature distribution. In this work, regions excluding large overhang features are often chosen as the EOC temperature location due to higher temperature variation associated with superelevated, heated metal.

4.2.3 Model Validation Error Metrics

It is necessary to define the error values between the model-predicted graph theory and the IR EOC temperatures to validate model results. Symmetric mean absolute percent error (SMAPE), root mean square error (RMSE), and mean absolute deviation (MAD) are listed in Table 4-2 below.

Table 4-2: Error metrics comparing model predictions to experimental IR data.

Error Metric	Equation	Rationale
Symmetric mean absolute percent error (SMAPE)	$SMAPE = 100\frac{1}{n}\sum_{t=1}^{n}\frac{\lvert F_t - A_t\rvert}{\lvert F_t\rvert + \lvert A_t\rvert}$ Where A_t are the actual values, F_t are the forecasted values, t is the timestep for each point, and n is the number of fitted points.	Provides prediction accuracy of a forecasting method in statistics.
Root mean squared error (RMSE)	$RMSE = \sqrt{\frac{1}{n}\sum_{i=1}^{n}(F_i - A_o)^2}$ Where F_i is the forecasted value, A_o is the actual value, and n is the number of fitted points.	Provides a measure of the quadratic mean of differences between forecasted and actual values.
Mean absolute deviation (MAD)	$MAD = \sum_{i=1}^{n}\lvert F_i - A_o\rvert$ Where F_i is the forecasted value, A_o is the actual value, and n is the number of fitted points.	Provides a measure of the average magnitude of errors between forecasted and actual values.

4.3 Model Predictive Process Control

Once baseline, uncontrolled thermal histories are obtained for each supporting strategy, process control is then applied to the unsupported and partially supported brackets. As shown in Figure 4-5, the core idea with this feedforward approach is to reduce heat buildup by modifying the process parameters applied to each layer. In this work, laser power and velocity are the primary control variables of interest, whereas dwell time, additional delay time added after lasing and before recoating, is used where necessary to better achieve the control target where appropriate. In this workflow, a target geometry is input to the control algorithm, a baseline EOC temperature is modelled, then the model algorithmically chooses a laser power and laser velocity parameter plan to minimize the mean absolute deviation between target temperature and its modelled EOC temperature. Additionally, a heuristic parameter grading strategy is applied to the model's suggested parameter plan to deter layerwise cracking or porosity associated with sharp changes in process parameters, which can drastically change meltpool characteristics [93].

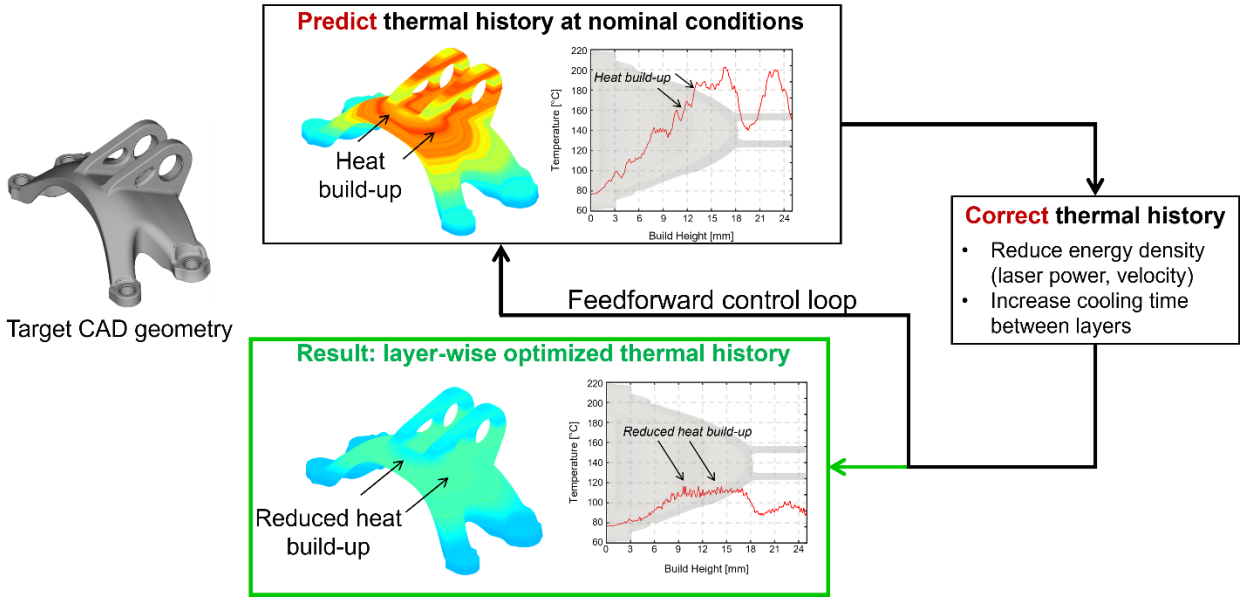

Figure 4-5: Graph theory feedforward thermal process control approach.

4.3.1 Process Control Parameter Choices

To algorithmically choose the laser power and laser velocity parameters, first, an acceptable set of parameters must be chosen based on experimental data: such is the purpose of the porosity DOE. It is important to note that a finite set of acceptable laser power-velocity (PV) combinations are down-selected and enabled as valid choices for process control; for this work, experimentally validated PVs are used directly. Additionally, if a larger parameter space was used as a model input, more time for computation would be required. Once performed, given percentage porosity and maximum pore dimension data for each designed PV combination, PVs failing the porosity requirements are excluded. Of the remaining porosity-acceptable PVs, minimal-energy density input parameters are chosen, as measured by Volumetric Energy Density (VED) as $VED = \frac{P}{\mathrm{v}\times\mathrm{h}\times\mathrm{t}}$ [J/mm^3], where P is the laser power [W], v is the laser scan speed [mm/s], h is hatch spacing [mm], and t represents layer thickness [mm] [94]. VED is used to down-select these parameters for both comparative purposes and to enable lowest energy input to maximally deter overheating within a porosity-acceptable parameter space.

4.3.2 Unsupported Controlled Bracket

The unsupported bracket's final controlled and uncontrolled EOC temperatures are shown in Figure 4-8. It is noted that a relatively large difference (approximately 50 to 100 °C) is shown for the uncontrolled versus controlled case, primarily attributed to the inclusion of a 20s minimum layer time enforced. This additional time was chosen to further reduce control error, as shown in Figure 4-6, which demonstrates the original process control output, without a minimum layer time enforced, up to approximately 50 °C from the target thermal history. This heuristic choice is based on the current estimated inter-layer time (ILT), as shown in Figure 4-7. Finally, shown in Figure

4-8, the additional cooling time added enabled convergence to the target thermal history. Additionally, inclusion of the [210 W, 1300 mm/s] PV combination further enabled lesser energy input than from the originally chosen acceptable set of PVs.

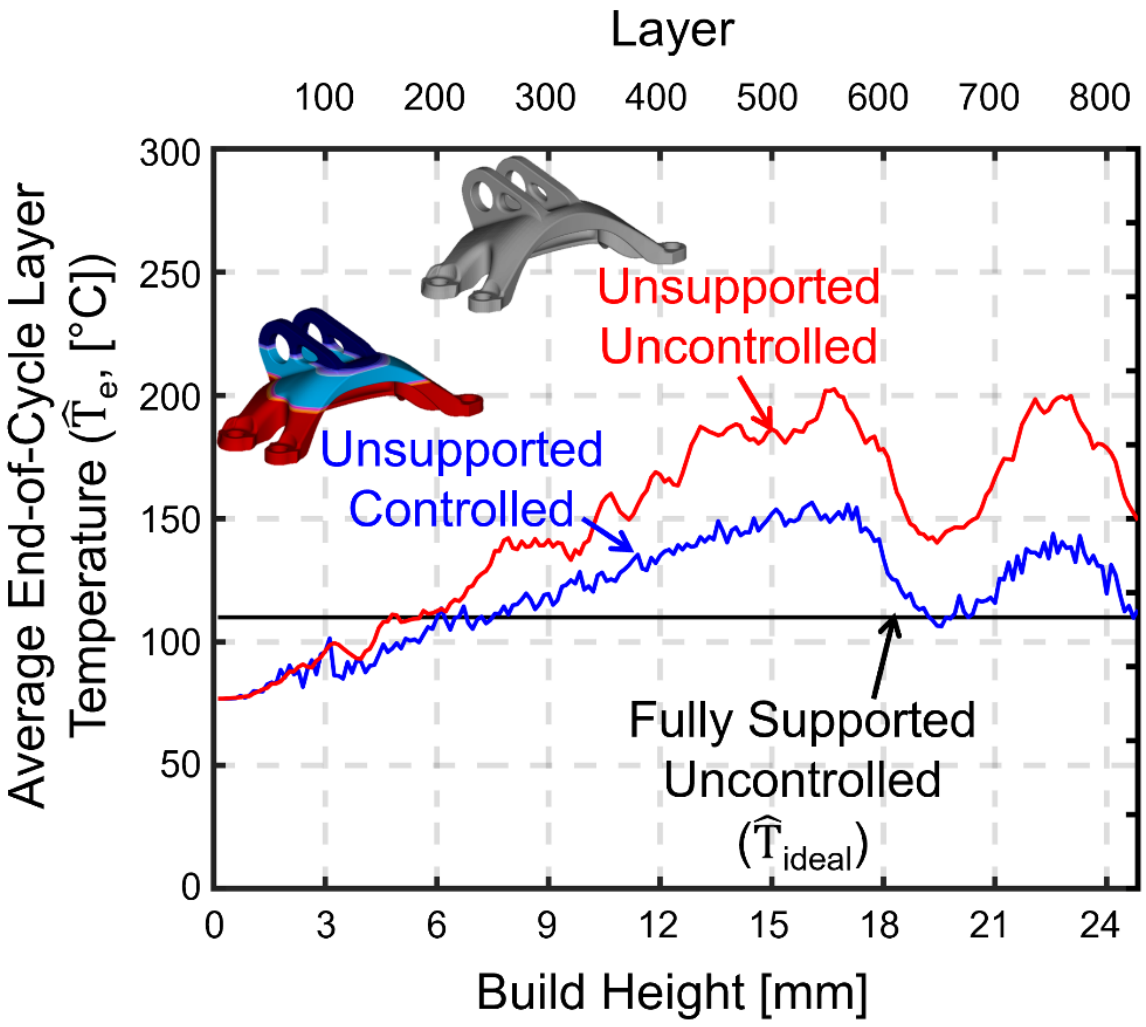

Figure 4-6: Original EOC temperatures for unsupported bracket control scheme.

This heuristic choice of a 20-second minimum layer time is based on the current estimated inter-layer time (ILT) profile, as shown in Figure 4-7. A constant, minimal layer time approach was used in this work instead of a model-determined dwell time strategy due to lack of machine control over layerwise dwell time; for the SLM 280 2.0, the user can only enforce a manually-set minimum layer time, so 20 seconds was chosen for the entire build. Another potential option would

be to print a zero-power "ghost" part to add ILT, but was not chosen due to difficulty of implementation.

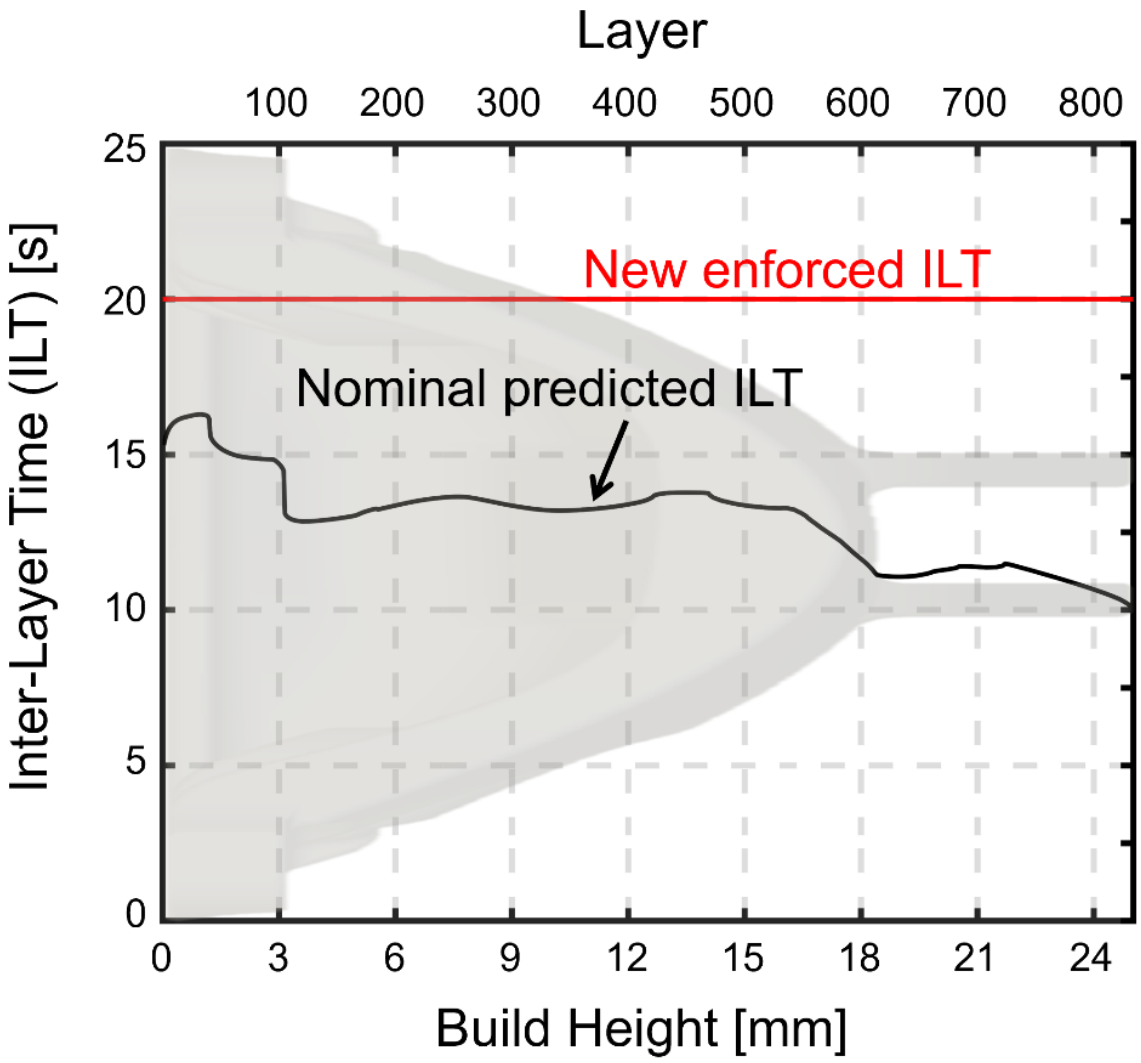

Figure 4-7: Original and modified inter-layer time (ILT) to reduce heat build-up.

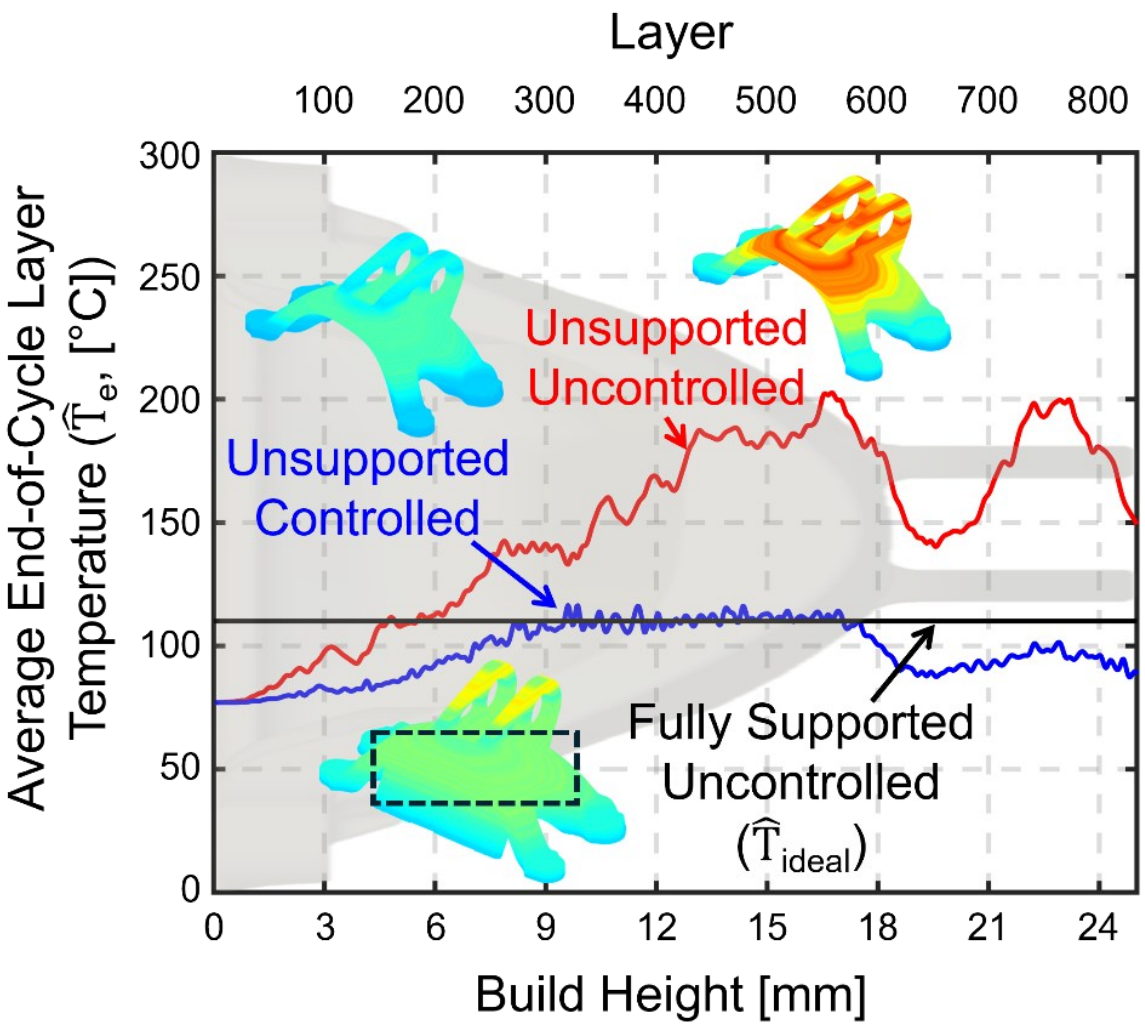

Figure 4-8: EOC temperatures for final unsupported bracket control scheme.

The process-controlled laser power and velocities, shown in Figure 4-9, illustrate the nominal PVs (210 W, 880 mm/s) with both the model-suggested PVs (plotted with diamond markers) and the graded PVs (plotted with small circle markers). It can be seen that smaller, stepwise PV changes are implemented in 8-layer increments; since the thermal simulation uses 4-layer thickness superlayers, this approach applies small changes over 2 superlayers. Additionally, since a superlayer approach is used to reduce model computation time by reducing the simulated layers by a factor of 4, a grading strategy may enable higher fidelity process parameter outputs without the additional time penalty of simulating small parameter changes. For the unsupported bracket

grading methodology, it is noted that intermediate points of [270 W, 1160 mm/s], [270 W, 1300 mm/s], and [210 W, 1020 mm/s] are not followed strictly; this is done to simplify the grading strategy and subsequent implementation. As shown in Figure 4-10, this choice enables more linear grading with respect to VED.

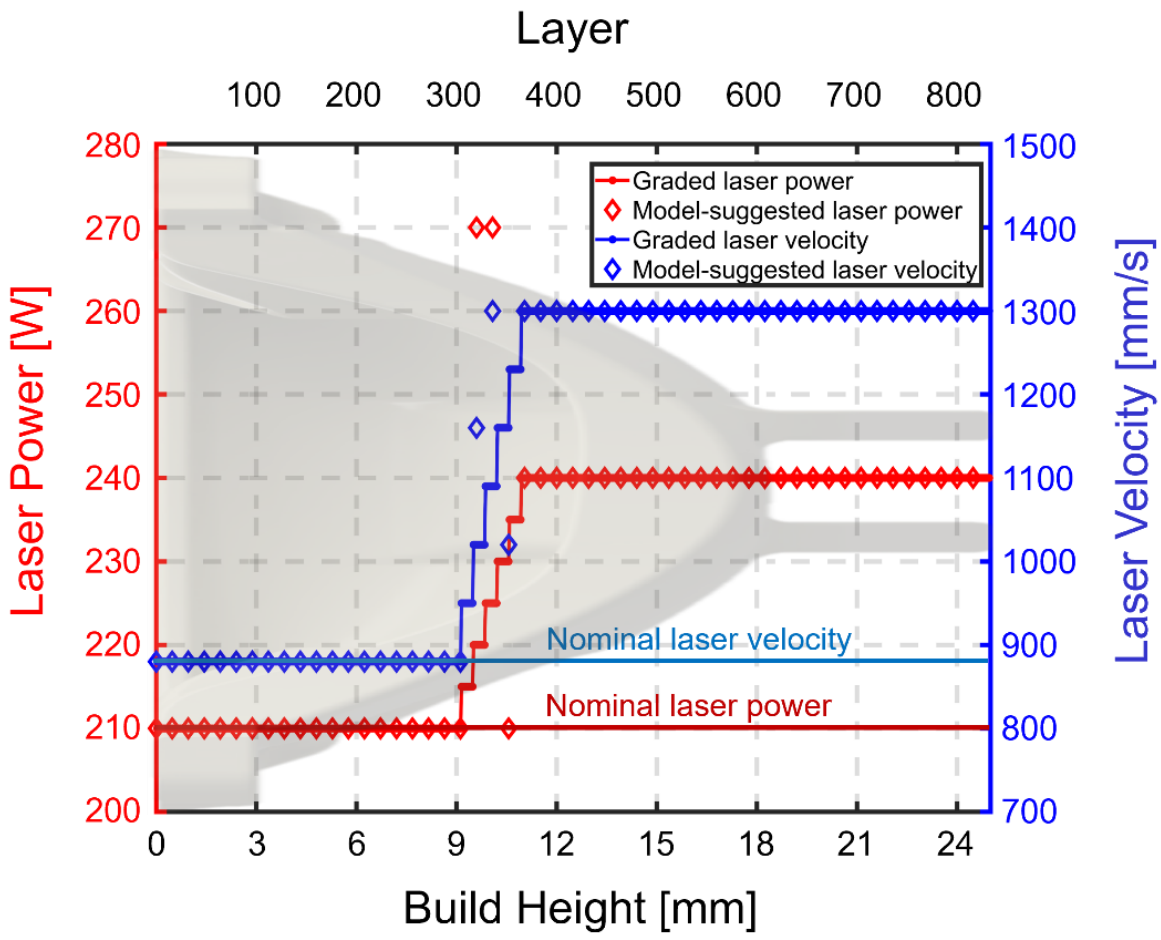

Figure 4-9: Unsupported bracket's model-suggested and graded laser power/velocities.

The motivation for applying graded PVs is shown in Figure 4-10. Rather than employing sharp parameter changes with a delta of approximately 10 J/mm^3 over a single layer, the grading strategy enables smaller VED changes (approximately 3-4 J/mm^3) over a longer set of layers (8 real layers, 2 superlayers) to deter large changes in meltpool characteristics which can induce porosity, cracking, or other unwanted layerwise part defects. It is noted that while VED is a useful

metric for comparing energy input as a function of process parameters, it does not capture the resulting effects on meltpool characteristics and thermal history of the process [94].

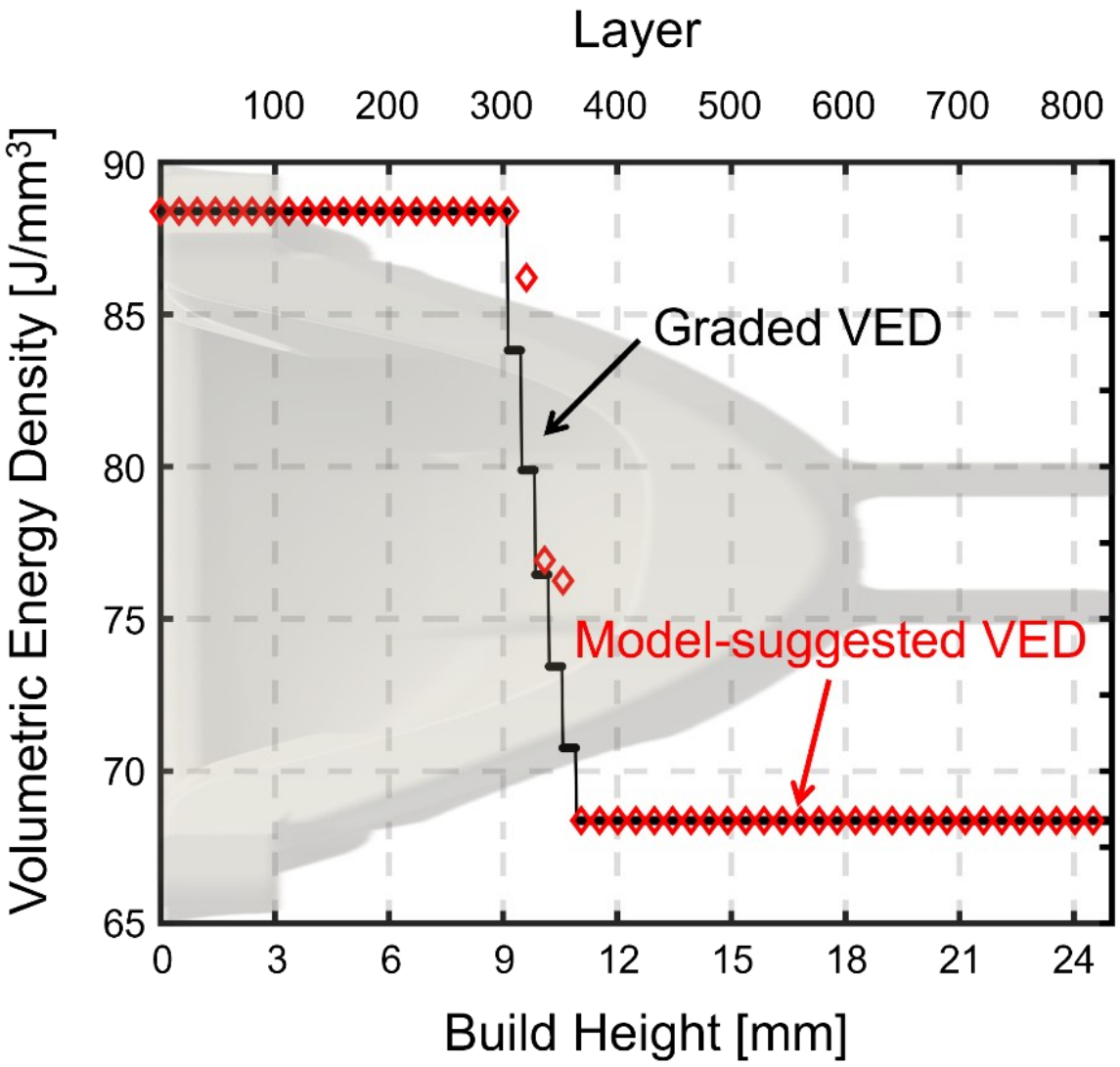

Figure 4-10: Volumetric energy density (VED) of model-suggested and graded strategies for the unsupported bracket.

4.3.3 Partial Supported Controlled Bracket

For the partially supported bracket, unlike the controlled bracket, a dwell time was not enforced, as its modelled process-controlled EOC temperatures showed reasonable agreement (less than 20 °C) with the chosen, constant target thermal history at the primary overhang features. For

this bracket, the [210 W, 1300 mm/s] PV combination was excluded. The uncontrolled and controlled partially supported bracket's EOC temperatures are shown in Figure 4-11.

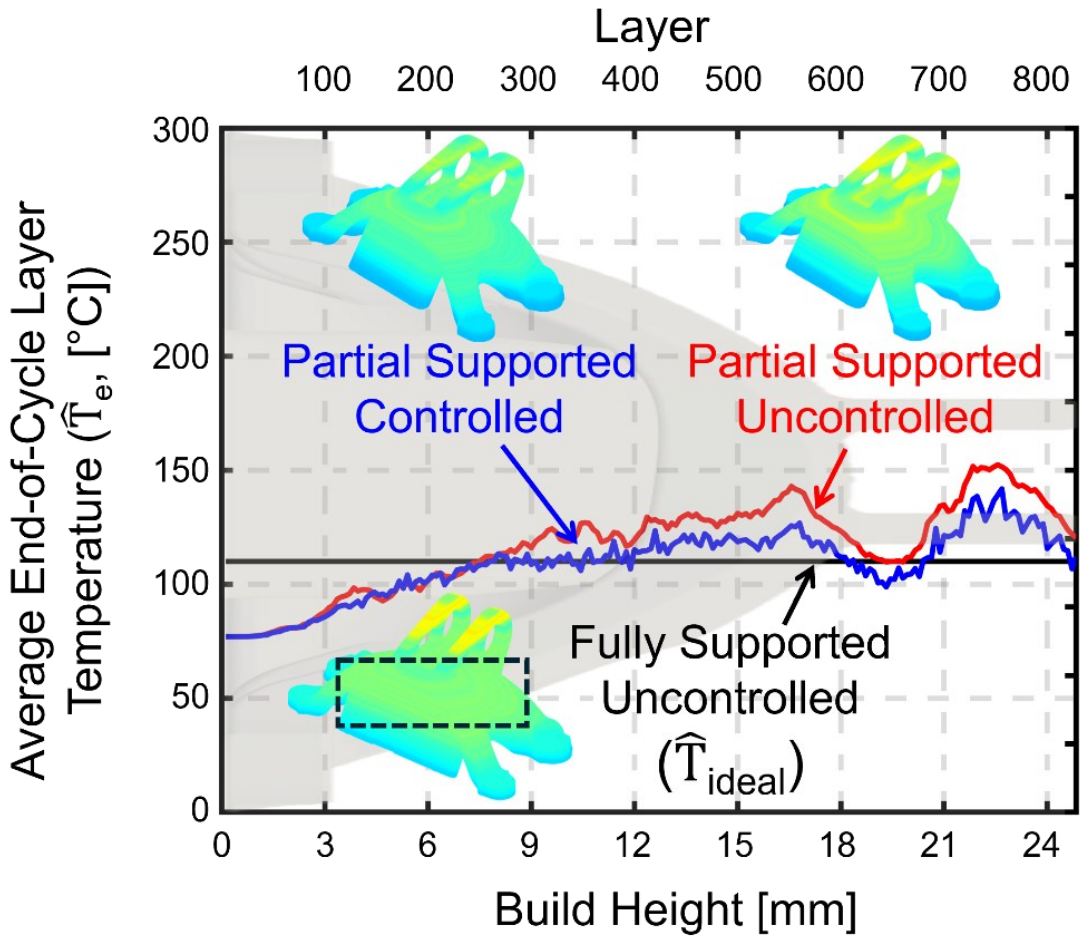

Figure 4-11: EOC temperatures for partially supported bracket control scheme.

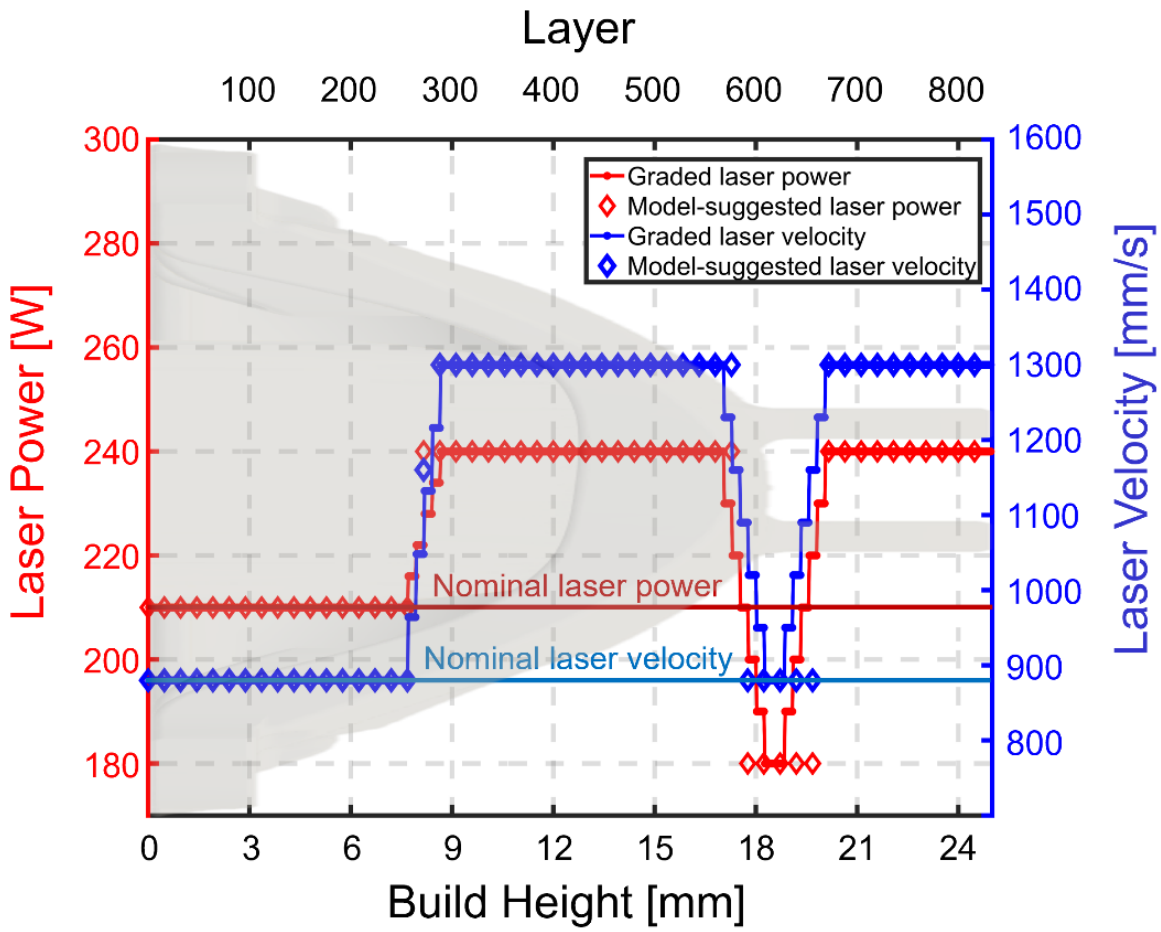

Figure 4-12: Partially supported bracket's model-suggested and graded laser power/velocities

A similar parameter grading strategy was employed for the partially supported bracket. Again, large VED changes (approximately 10 J/mm^3) over a single layer are reduced to smaller VED changes (approximately 3-4 J/mm^3) over 8 real layers. All intermediate PV combinations are considered for this bracket as there are two primary regions of VED changes at the major overhang feature and for the topmost pin connection feature.

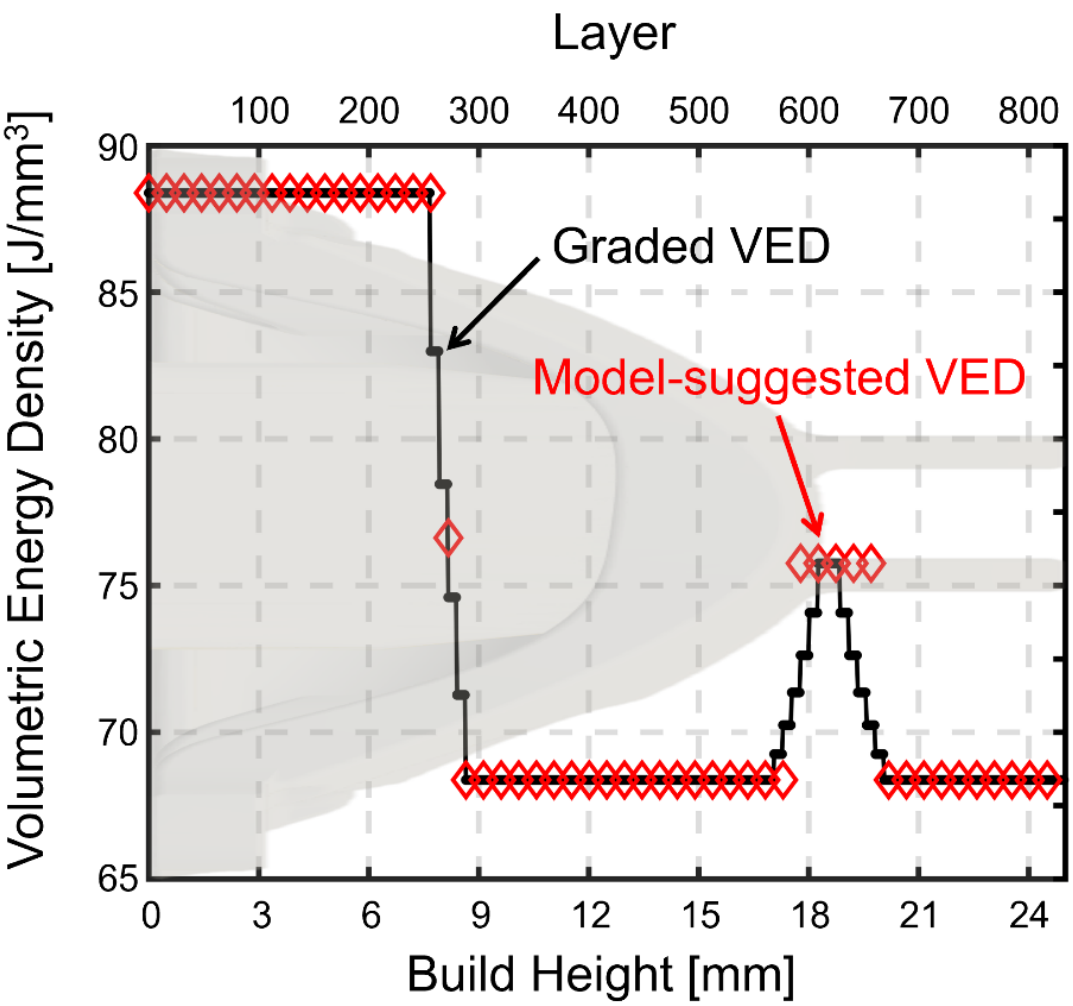

Figure 4-13: Volumetric energy density (VED) of model-suggested and graded strategies for the partially supported bracket.

5 Results

5.1 Process Window

The goal of the porosity DOE is to determine porosity-acceptable PV combinations for process control implementation. From the microscope analysis, density and large pore data was overlaid on each PV combination to determine a PV process map, shown in Figure 5-1. Upon inspection of each sample, nearly every sample exhibited some form of porosity; in this work, LOF porosity is more important, as it is more likely to violate the porosity requirements. However, many samples exhibited keyhole porosity, characterized by many small pores, which still pass the porosity requirements. In this work, lower VED, non-LOF parameters are more desirable, as they are conducive to reducing heat build-up. One insight gained is that keyhole porosity is not as undesirable as LOF porosity, so it could be leveraged for larger part applications to maximize productivity.

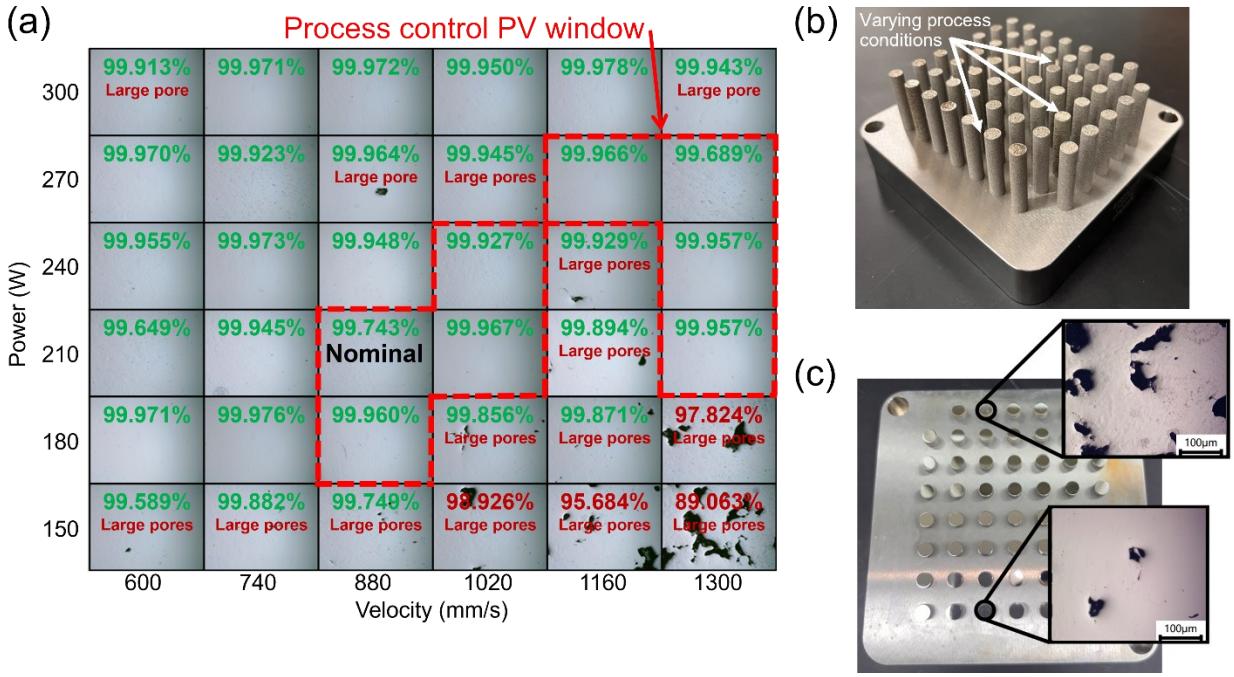

Figure 5-1: Process window results. (a) Process control PV window with overlaid density and large pores data. (b) As-printed pin specimens. (c) Post-processed pin specimens.

5.1.1 Parameter Selection and Rationale

As depicted in Figure 5-1, the nominal hatch PV was chosen to allow for a wider range of PV selections for the model-determined parameter plan as compared to SLM's suggested nominal of [240 W, 1000 mm/s]. The sample corresponding to [210 W, 880 mm/s] passed the porosity requirements and has nearly identical VED compared: 88.88 J/mm^3 and 88.38 J/mm^3, respectively. Upon exclusion of PVs violating the porosity requirements, the VED-minimal parameters were chosen. For example, 240 W, 740 mm/s meets the porosity requirements, but has a VED of 120.12 J/mm^3, so simulation of this PV is redundant as the model would choose lower VED PVs instead to reduce heat build-up. The down-selected, allowed PV combinations for PVs, shown in Table 5-1 below, demonstrate how VED was used as a comparator to establish the process control PV window.

Table 5-1: PV combinations used in the process control algorithm.

PV Combination	Volumetric Energy Density [J/mm^3]
210W, 880 mm/s	88.38
240W, 1020 mm/s	87.15
270W 1160 mm/s	86.21
270W, 1300 mm/s	76.92
210W, 1020 mm/s	76.25
180W, 880 mm/s	75.76
240W, 1300 mm/s	68.38
210W, 1300 mm/s	59.83

5.1.2 Limitations

It is noted that [210 W, 1300 mm/s] PV set was used in the unsupported bracket, but not for the partially supported bracket. This decision was made in order to (a) improve reduction in heat build-up in addition to dwell time added and (b) is appropriate for select overheating regions due to porosity defect healing phenomenon [95]. Upon closer examination of the PV process control window, it can be seen that both [240 W 1160 mm/s] and [210 W 1160 mm/s] are not porosity-

acceptable, but [240 W 1300 mm/s] and [210 W 1300 mm/s] are. It would be expected that, if LOF porosity is present, a lower VED PV set would also incur the same, if not more LOF porosity. This is likely due to sample-to-sample porosity variation inherent to a relatively small (5mm) sample diameter, but also that a single layer was inspected, rather than in a plane perpendicular to the build direction (XZ or YZ plane) in order to accelerate microscope and porosity characterization time. This sample-inherent variation, combined with LPBF-specific process variation, a key deterrent to its adoption [96], further combine to cause unexplained porosity variation within samples.

5.2 Thermal History and Part Quality Results

5.2.1 Fully Supported Uncontrolled Bracket

In Figure 5-2(a), the graph theory model's EOC temperature prediction is graphically compared to the experimental IR EOC temperatures. Notably, it can be seen that the graph theory result accurately predicts the thermal history within 5% SMAPE and 12 °C RMSE of verified IR results. Figure 5-2(b) and (c) visually depict an interpolated, layerwise representation of the EOC trends presented in Figure 5-2(a). Small discrepancies are visible at the topmost pin connection feature as well as near the front lip overhang feature. Most importantly, the accurate prediction of this part serves as verification of the heuristically chosen 110 °C target temperature for subsequent process-controlled builds.

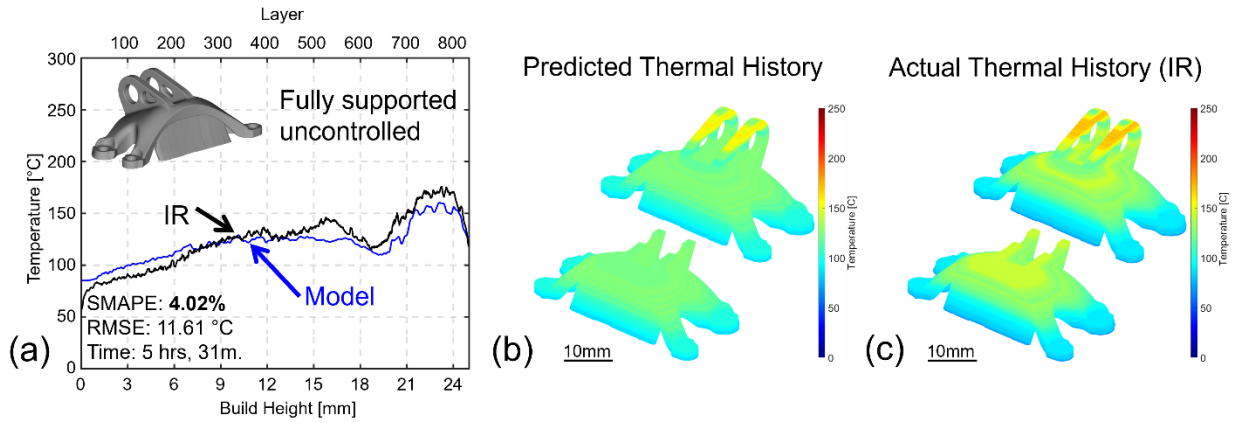

Figure 5-2: Predicted and actual thermal history results for the fully supported bracket. (a) Graph theory model and IR EOC trends vs build height. (b) Visual depiction of predicted EOC temperatures. (c) Visual depiction of IR EOC temperatures.

Upon printing and support machining operations, the fully supported bracket was 3D-scanned to serve as a part quality and geometric accuracy reference for subsequent builds, expected to incur higher geometric deviation and overheating. Figure 5-3 shows the as-printed bracket and 3D-scanned bracket, with close-up images of the critical regions above and below the primary part overhang. As seen in Figure 5-3(a) and (b), it can be seen that the topmost surface is smooth and built without any significant defects. Additionally, in Figure 5-3 (c), qualitatively, a small degree of charring and surface roughness is visible under the primary overhang, evidenced by Figure 5-3(d).

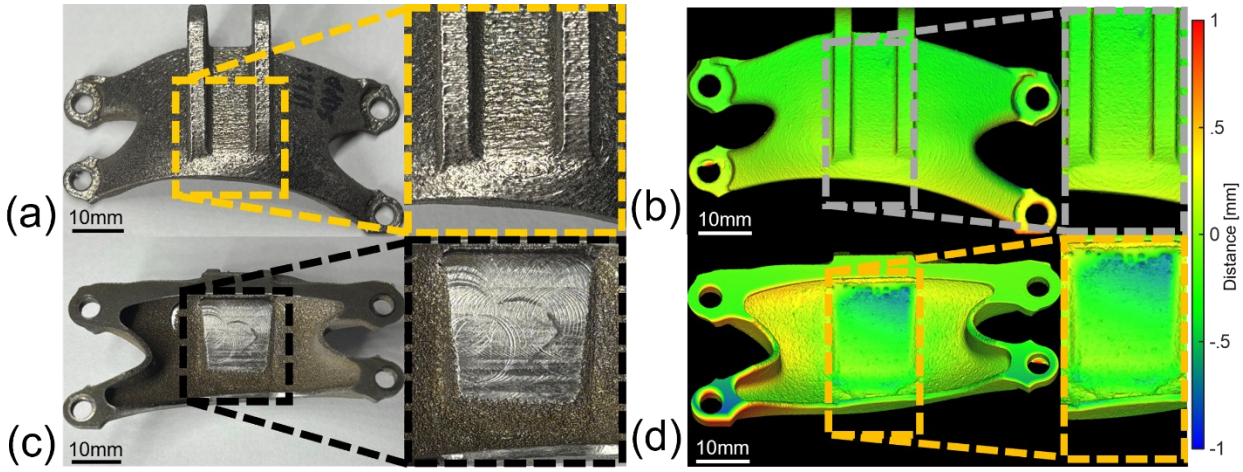

Figure 5-3: As printed and 3D-scanned fully supported bracket. (a) Top view of as-printed bracket. (b) Top view of 3D-scanned bracket. (c) Bottom-up view of as-printed bracket with as-machined support interface. (d) Bottom-up view of 3D-scanned bracket.

5.2.2 Unsupported Uncontrolled Bracket

Figure 5-4(a) demonstrates prediction of the unsupported uncontrolled bracket's thermal history within 4% SMAPE and approximately 12 °C RMSE. Without process control and without heat dissipative supporting structures, this bracket geometry generates significant heat build-up, demonstrated by the visuals in Figure 5-4(b) and (c) with both the primary overhang and the pin connection overhang feature nearing 200 °C maximums of their EOC temperatures.

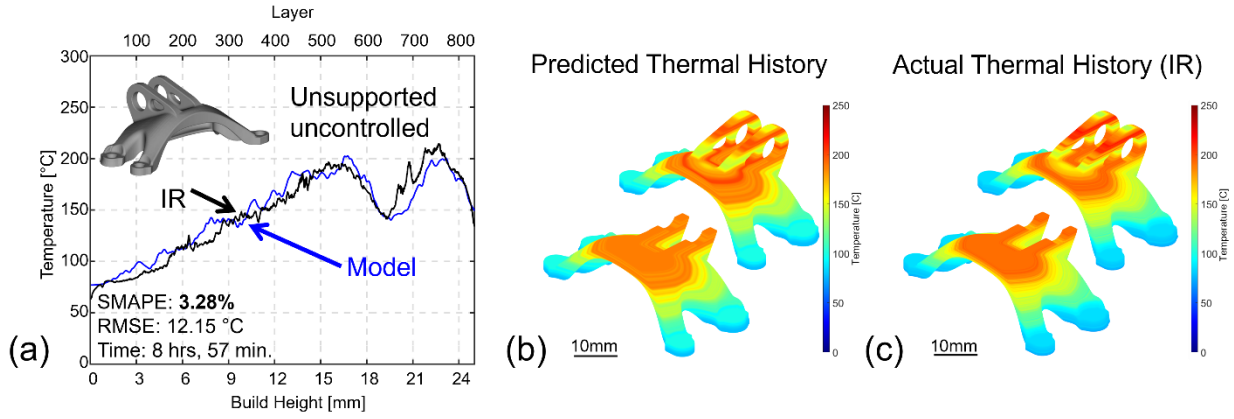

Figure 5-4: Predicted and actual thermal history results for the unsupported uncontrolled bracket. (a) Graph theory model and IR EOC trends vs build height. (b) Visual depiction of predicted EOC temperatures. (c) Visual depiction of IR EOC temperatures.

As expected with an aggressive (25° from horizontal) overhang, this bracket heated up significantly due to lack of necessary heat transfer pathways, which directly caused superelevation of the part structure during the print process, indicated by recoater streaks evidenced in Figure 5-5 below.

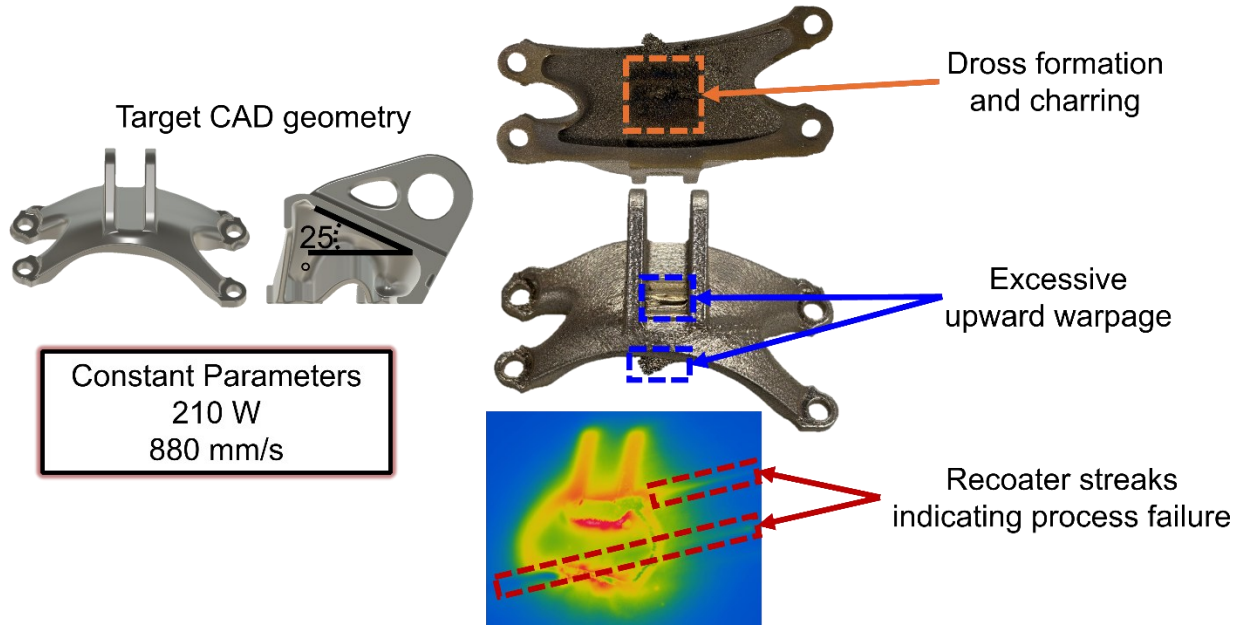

Figure 5-5: Poor part quality indicators of the unsupported uncontrolled bracket.

Inspecting further, in Figure 5-6, the bracket shows extreme (more than 1mm) geometric distortion. Excessive upward distortion is seen in Figure 5-6(a) and (b), indicated by fusiform-shaped defects on the topmost part surface. In Figure 5-6(c) and (d), roughness and dross are shown under the overhang feature exceeding 1mm.

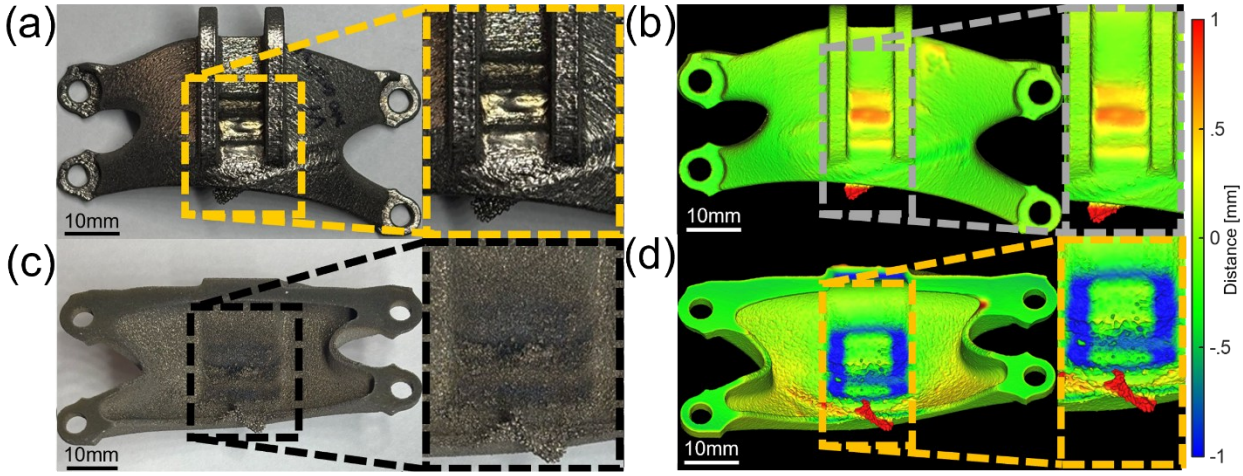

Figure 5-6: As printed and 3D-scanned unsupported uncontrolled bracket. (a) Top view of as-printed bracket. (b) Top view of 3D-scanned bracket. (c) Bottom-up view of as-printed bracket with as-machined support interface. (d) Bottom-up view of 3D-scanned bracket.

5.2.3 Unsupported Controlled Bracket

With process control applied and dwell time added, the unsupported controlled bracket significantly reduced heat build-up, as shown in Figure 5-7(a), nearly one half of the 200 °C peaks seen in the uncontrolled bracket. As intended, the middle part of the bracket (~9 to 18 mm of build height) were built approximately at the 110 °C temperature target, as seen in Figure 5-7 (b) and (c) with good agreement (~4% SMAPE and ~9 °C RMSE).

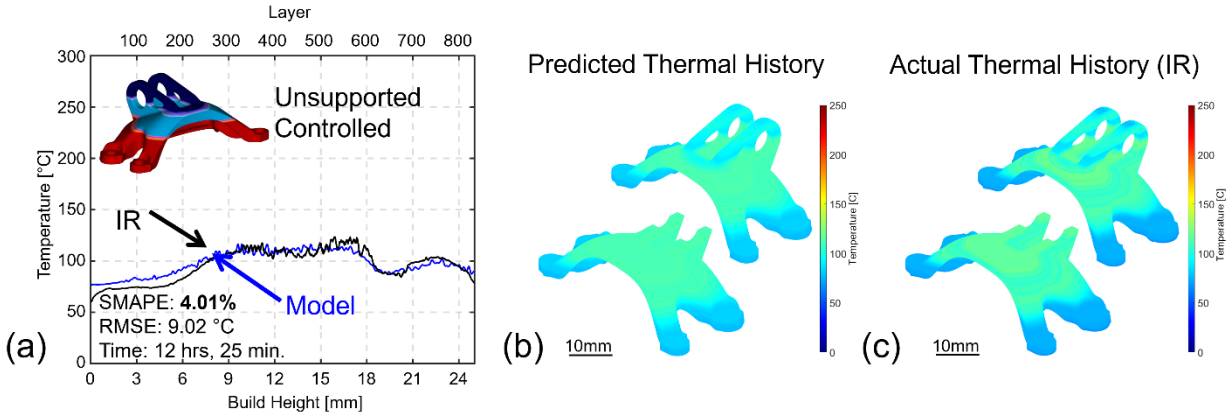

Figure 5-7: Predicted and actual thermal history results for the unsupported controlled bracket. (a) Graph theory model and IR EOC trends vs build height. (b) Visual depiction of predicted EOC temperatures. (c) Visual depiction of IR EOC temperatures.

Compared to its uncontrolled counterpart, the unsupported controlled bracket demonstrates improved part quality as measured by geometric deviation, although not immediately obvious. Excessive upward distortion also was incurred in this instance, but was less pronounced on the top-facing surface, seen in Figure 5-8(a) and (b); the uncontrolled part had three distinct upward bumps, and with greater geometric deviation (0.41 mm from 0.52 mm for the uncontrolled bracket). The dross and surface roughness was also slightly improved, qualitatively, as evidenced in Figure 5-8(c) and (d).

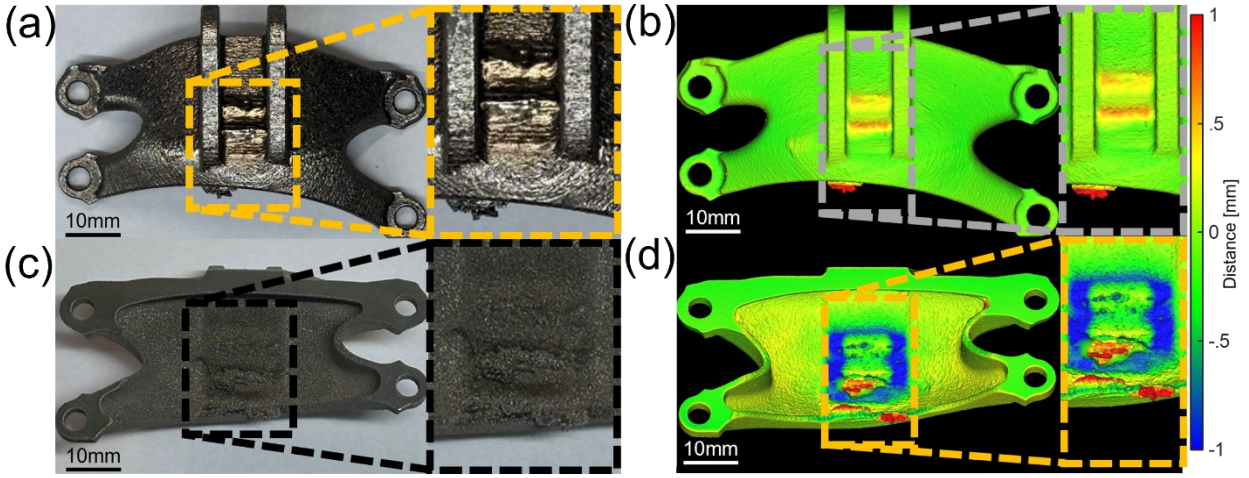

Figure 5-8: As printed and 3D-scanned unsupported controlled bracket. (a) Top view of as-printed bracket. (b) Top view of 3D-scanned bracket. (c) Bottom-up view of as-printed bracket with as-machined support interface. (d) Bottom-up view of 3D-scanned bracket.

5.2.4 Partially Supported Uncontrolled Bracket

With supporting structures added, the additional material to transfer heat away from the partially supported bracket led to decreased build risk and lower peak EOC temperatures, as shown in Figure 5-9 (a). The EOC temperature was predicted within 3% SMAPE and nearly 7 °C RMSE, shown visually in Figure 5-9(b) and (c).

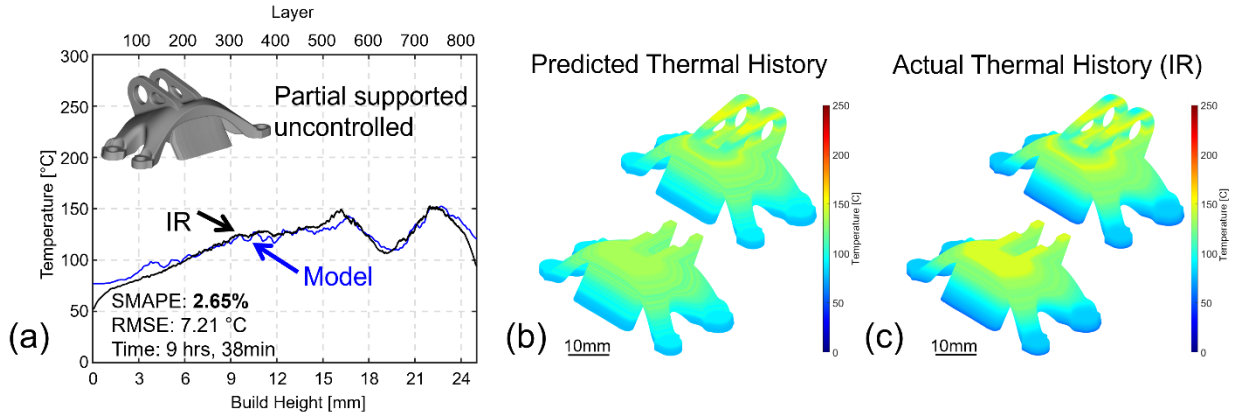

Figure 5-9: Predicted and actual thermal history results for the partially supported uncontrolled bracket. (a) Graph theory model and IR EOC trends vs build height. (b) Visual depiction of predicted EOC temperatures. (c) Visual depiction of IR EOC temperatures.

Due to the addition of supporting structures, part quality is increased for the partially supported bracket, even in an uncontrolled case. Shown in Figure 5-10(a) and (b), only one, smaller

upward bump is observed, as compared to three, relatively large ones for the unsupported uncontrolled bracket. Due to the support on the front lip geometry, there was no significant geometric deviation observed at this feature. A small degree of roughness and dross formation is visible adjacent to the machined surface in Figure 5-10(c) and (d).

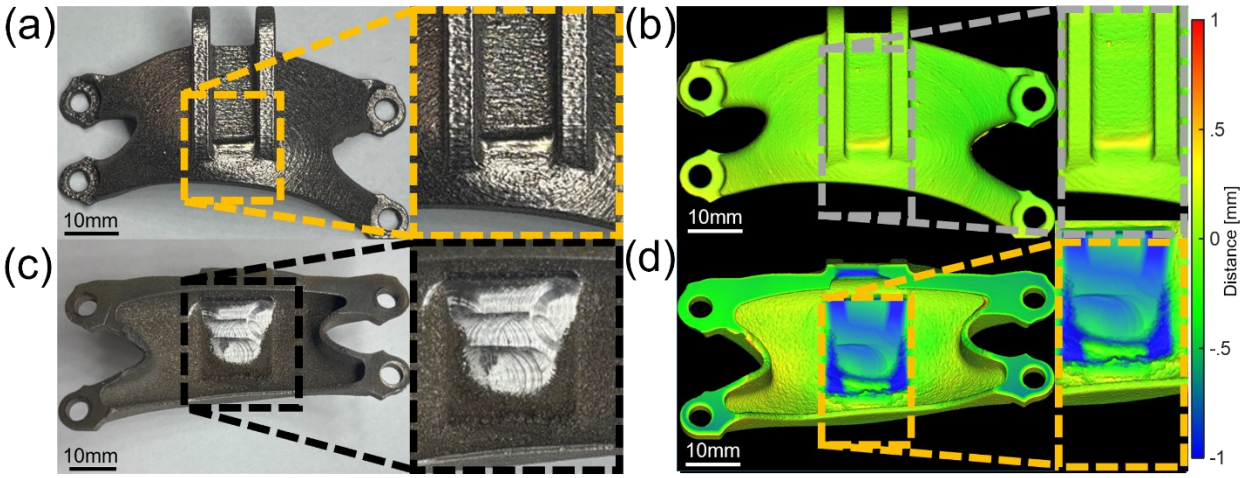

Figure 5-10: As printed and 3D-scanned partially supported uncontrolled bracket. (a) Top view of as-printed bracket. (b) Top view of 3D-scanned bracket. (c) Bottom-up view of as-printed bracket with as-machined support interface. (d) Bottom-up view of 3D-scanned bracket.

5.2.5 Partially Supported Controlled Bracket

With process control, the partially supported bracket again showed good agreement (~3% SMAPE, ~9 °C RMSE) to its predicted EOC temperatures, shown in Figure 5-11. The small discrepancies visible in Figure 5-11(a) are visually depicted in Figure 5-11(b) and (c).

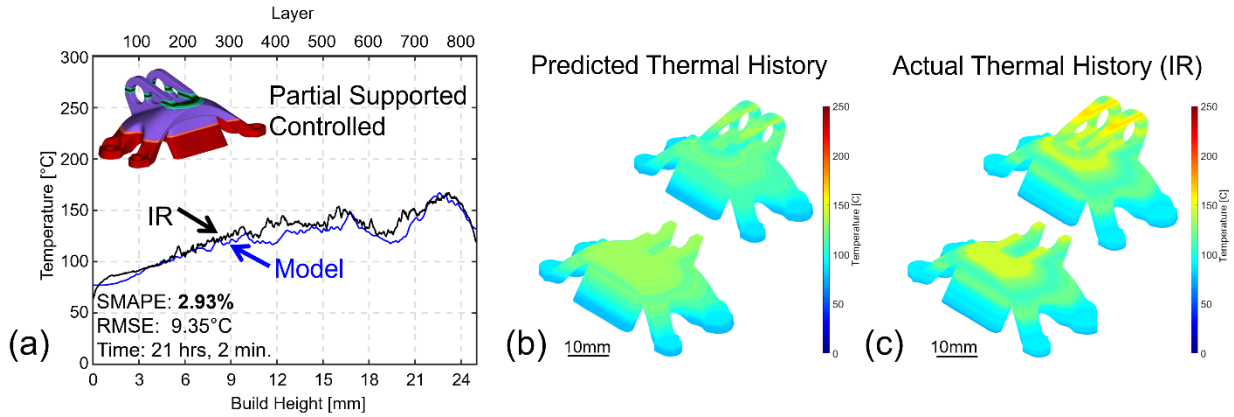

Figure 5-11: Predicted and actual thermal history results for the partially supported controlled bracket. (a) Graph theory model and IR EOC trends vs build height. (b) Visual depiction of predicted EOC temperatures. (c) Visual depiction of IR EOC temperatures.

Compared to its uncontrolled counterpart, the controlled partially supported bracket eliminated the upward bump defect shown previously: there were no visible recoater streaks visible during the print process, as demonstrated in Figure 5-12(a) and (b). A similar degree of charring and roughness is visible in Figure 5-12(c) and (d).

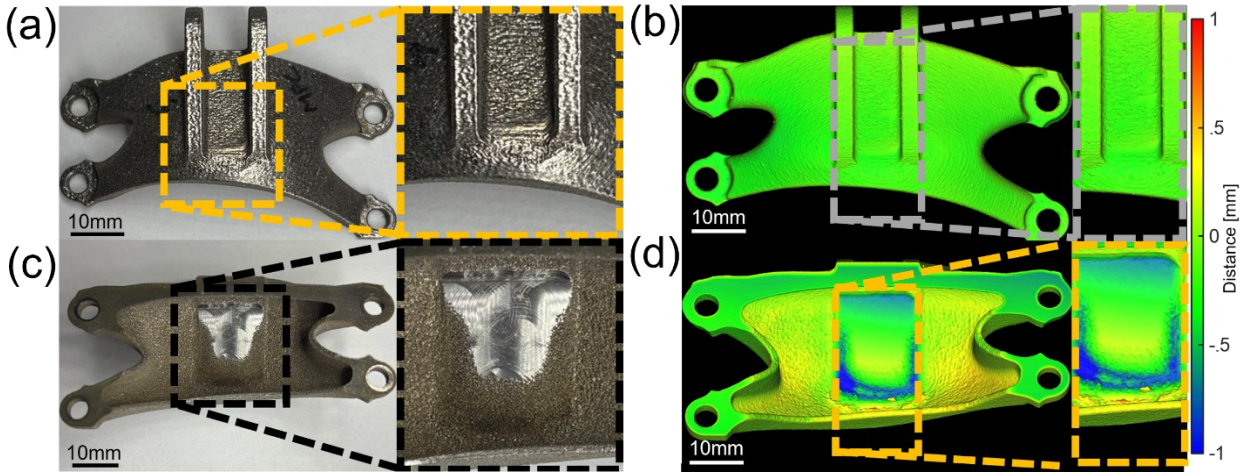

Figure 5-12: As printed and 3D-scanned partially supported controlled bracket. (a) Top view of as-printed bracket. (b) Top view of 3D-scanned bracket. (c) Bottom-up view of as-printed bracket with as-machined support interface. (d) Bottom-up view of 3D-scanned bracket.

5.2.6 Summary

Shown in Table 5-2, all EOC temperatures were predicted within 5% SMAPE. Additionally, all brackets' mean absolute deviation (MAD) was observed to be less than 10 °C.

Table 5-2: Thermal history prediction results summary.

	SMAPE (%)	RMSE (°C)	MAD (°C)
Fully Supported Uncontrolled	4.03	11.61	9.65
Unsupported Uncontrolled	3.28	12.15	9.38
Unsupported Controlled	4.01	9.02	7.68
Partial Supported Uncontrolled	2.65	7.21	5.57
Partial Supported Controlled	2.97	8.43	6.89

As measured from each part's 3D scan compared to its target geometry geometric deviations are presented in Table 5-3. Due to lack of consistent measurement tools within the CloudCompare software, each of the values presented are the average of three human-verified measurement points, which add variability to these quantitative results. Additionally, the front lip distortion is measured at the bottom-facing surface of the front lip feature; in the fully supported and all partially supported parts, this feature is measured from a machined surface, not on an as-printed surface. The large overhang feature is measured on the topmost surface of the part between the pin connection parallel features. Therefore, on as-printed surfaces, improvement in geometric deviation is seen for the unsupported bracket in the front lip (0.52 mm from 0.61 mm) and the large overhang (0.41 mm from 0.51 mm). Improvement is also seen for the partially supported bracket's large overhang feature (-0.17 mm from 0.22 mm).

Table 5-3: Approximate feature-specific geometry deviations

	Front lip distortion (mm)	Large overhang distortion (mm)
Fully Supported Uncontrolled	-0.23	-0.07
Partial Supported Uncontrolled	0.03	0.22
Partial Supported Controlled	0.32	-0.17
Unsupported Uncontrolled	0.61	0.51
Unsupported Controlled	0.52	0.41

6 Conclusions and Future Work

In this work, feedforward control of an LPBF thermal model was applied to a complex aerospace component fabricated with IN718. Over varying support levels, the process control algorithm was deployed to mimic the thermal history of a well-supported part to promote higher part quality. Additionally, this algorithm enables thermal history- and geometry-based laser power and laser velocity parameters, critical to reduce the need for costly, empirical build-and-test approaches. Demonstrated in this work is that process control improved part quality for all brackets. For the partially supported bracket, process control eliminated process failures and distortion defects, while reducing necessary support structure volume by 45%, and equivalently, overall part and support volume by 19% solely through support reduction, not through part design.

6.1 Contributions

The specific contributions of this thesis are as follows:

(1) The thermal model and process control was applied to a complex geometry – a key missing element in literature. Despite the thin walls, curved features, and aggressive overhangs that can complicate part-level simulation, the thermal history, interpreted as its EOC temperature, was predicted within 5% SMAPE and 10 °C MAD.

(2) Process control eliminated part defects and process failures exemplified through part-recoater interactions. Since process control printed the partially supported bracket to similar quality of the fully supported bracket as measured by geometric distortion, this method enabled support design optimization by reducing necessary support structure volume by 45%.

(3) Compared to laser power control approaches in literature, the process control strategy employed varying laser power, velocity, and dwell time. Key to this methodology is that

process control *autonomously* generates a layerwise parameter plan, useful towards considerations of both the parameter choices and their locations – especially useful for a complex geometry, likely at overhang features.

(4) To the best of the authors' knowledge, a VED grading methodology has not been shown in prior literature. Using the model's suggested output parameter plan, a heuristic parameter grading strategy was employed to make smaller VED changes over a longer set of layers, rather than incur layerwise defects associated with sharp meltpool characteristic changes. So, the authors suggest, that for layerwise parameter grading, approximately 5 J/mm^3 over 5-10 layers is likely sufficient to deter undesired part defects associated with meltpool and thermal-induced effects.

6.2 Limitations

A major limitation of this work lies in the determination of the PV process window. Currently, the main approaches for determining porosity-acceptable process parameters is through printing density coupons (constant cross-sectional shape, typically a cube or cylinder), or by printing the final geometry with an initial guess of parameters, evaluating porosity and iterating; the former was chosen for this work to minimize costs and build time while accelerating porosity characterization time. Additionally, only a single layer perpendicular to the build direction (XY plane, instead of YZ or XZ plane) was analyzed which incurs additional variation in the porosity results, evidenced by porosity-unacceptable PVs with adjacent porosity-*acceptable* PVs with lower VED, against expectation. Compared to the layerwise microscope analysis performed, CT scanning to derive porosity results would be much more preferred, as all layers' porosity (~850 layers) is a much larger sample size than the 1-2 layers analyzed in this work. This reduced sample

size, in turn, incurred more variability in the porosity DOE results – lower VED sample counterintuitively had acceptable porosities than a higher VED one.

Ultimately, these parameter studies intend to remove the effect of geometry on the parameters' output performance metrics but is highly difficult to replicate without either (a) a high-fidelity, hatch-level final part simulation or (b) prints of the final part, evaluation, then parameter iterations. So, the process window was approximated for this work; the true process window is not necessarily shown as it is geometry and feature-specific. Within the LPBF process, heat transfer boundary conditions change locally with respect to geometries, so a refined process control approach is needed for thin-wall and steep overhangs to maintain a stable manufacturing process.

Additionally, a bracket build excluded from this work was used to calibrate the graph theory heat transfer coefficients with respect to adjacent powder, convection, and conduction to the build plate. While similar heat transfer coefficients can be somewhat geometrically-transferable across the same material, the final, calibrated heat transfer coefficients are unique to each machine, material, and geometry combination.

Part quality is solely evaluated in this work through post-print 3D scans of the external part geometry. In reality, to evaluate the fitness of this part for its application, internal characterization of this part should be performed to address considerations of excess porosity, chemical composition, tensile strength and all properties necessary for end-use part qualification.

Generalizability limitations are also noted to address practical concerns of implementation. In terms of the graph theory thermal model, accurate (<10% error) results are typically material- and machine-specific due to changes in machine heat transfer boundary conditions and material properties affecting heat diffusion. However, calibration of the heat transfer coefficients with

respect to substrate heat loss, surrounding powder heat loss, and convective heat loss sometimes require recalibration for unique part geometries; in other words, the graph theory thermal model is *somewhat* geometry-specific. However, relatively similar geometries may not require major heat transfer coefficient changes to achieve accurate results. Ultimately, simulation of a first-principles formulated discrete heat diffusion equation enables the model to capture overall thermal history trends with calibration of simulation parameters to simulate and validate accurate results.

6.3 Future Work

Due to current build file preparation software, machine, and modelling limitations, within-layer parameter changes were not employed in this work; within-layer, rather than layerwise parameter changes, should be implemented to reduce the minimum overhang angle of LPBF parts and further inhibit excess distortion associated with overheating. Additionally, due to lack of machine access to real-time process parameter control, feedback control was not performed and deemed outside the scope of this work. Finally, to more comprehensively evaluate part quality, internal part characterization will be performed: 3D porosity distribution and pore size using CT scanning, microstructure (PDAS, grain structure), hardness, and fracture strength.

References

1. Riensche, A., et al., *DynamicPrint: A physics-guided feedforward model predictive process control approach for defect mitigation in laser powder bed fusion additive manufacturing.* Additive Manufacturing, 2025. **97**: p. 104592.
2. Kladovasilakis, N., et al., *Influence of Selective Laser Melting Additive Manufacturing Parameters in Inconel 718 Superalloy.* Materials, 2022. **15**(4): p. 1362.
3. *5541 Boeing Baseline Delta Qualification Program*. 2025; Available from: https://www.americamakes.us/projects/5541-boeing-baseline-delta-qualification-program/.
4. Yavari, R., et al., *Part-scale thermal simulation of laser powder bed fusion using graph theory: Effect of thermal history on porosity, microstructure evolution, and recoater crash.* Materials & Design, 2021. **204**: p. 109685.
5. Malý, M., et al., *Effect of high-temperature preheating on pure copper thick-walled samples processed by laser powder bed fusion.* Journal of Manufacturing Processes, 2022. **73**: p. 924-938.
6. Le, V.T. and Y. Quinsat, *In situ calibration of galvanometric scanning head for laser powder bed fusion machines based on a vision system.* The International Journal of Advanced Manufacturing Technology, 2020. **111**(5): p. 1767-1783.
7. Chen, C., et al., *Microstructure evolution and mechanical properties of laser additive manufactured Ti6Al4V alloy under nitrogen-argon reactive atmosphere.* Materials Science and Engineering: A, 2022. **841**: p. 143076.
8. Calta, N.P., et al., *Pressure dependence of the laser-metal interaction under laser powder bed fusion conditions probed by in situ X-ray imaging.* Additive Manufacturing, 2020. **32**: p. 101084.
9. Bevans, B.D., et al., *Digital twins for rapid in-situ qualification of part quality in laser powder bed fusion additive manufacturing.* Additive Manufacturing, 2024. **93**: p. 104415.
10. Abd-Elaziem, W., et al., *On the current research progress of metallic materials fabricated by laser powder bed fusion process: a review.* Journal of Materials Research and Technology, 2022. **20**: p. 681-707.
11. Mercurio, V., et al., *Increasing of production rate of laser powder bed fusion systems.* Procedia CIRP, 2023. **118**: p. 699-704.
12. Zhang, L., Y. Li, and H. Zhu, *Prediction and optimization of dimensional accuracy of inclined structures fabricated by laser powder bed fusion.* Journal of Manufacturing Processes, 2022. **81**: p. 281-289.
13. Whip, B., L. Sheridan, and J. Gockel, *The effect of primary processing parameters on surface roughness in laser powder bed additive manufacturing.* The International Journal of Advanced Manufacturing Technology, 2019. **103**(9): p. 4411-4422.
14. Kasprowicz, M., et al., *Ways to increase the productivity of L-PBF processes.* Archives of Civil and Mechanical Engineering, 2023. **23**(3): p. 211.
15. Pradeep, P.I., et al., *Processing and Characterization of 3D-Printed Inconel-718 Component through Laser Powder Bed Fusion Route for High-Temperature Space Application.* Transactions of the Indian National Academy of Engineering, 2021. **6**(1): p. 133-146.
16. Arena, M., et al., *Design and Qualification of an Additively Manufactured Manifold for Aircraft Landing Gears Applications.* Aerospace, 2023. **10**(1): p. 69.

17. Puttonen, T., et al., *Influence of feature size and shape on corrosion of 316L lattice structures fabricated by laser powder bed fusion.* Additive Manufacturing, 2023. **61**: p. 103288.

18. Gradl, P., et al., *Robust Metal Additive Manufacturing Process Selection and Development for Aerospace Components.* Journal of Materials Engineering and Performance, 2022. **31**(8): p. 6013-6044.

19. Bendsoe, M.P. and O. Sigmund, *Topology optimization: theory, methods, and applications*. 2013: Springer Science & Business Media.

20. Bendsøe, M.P. and N. Kikuchi, *Generating optimal topologies in structural design using a homogenization method.* Computer methods in applied mechanics and engineering, 1988. **71**(2): p. 197-224.

21. Ibhadode, O., et al., *Topology optimization for metal additive manufacturing: current trends, challenges, and future outlook.* Virtual and Physical Prototyping, 2023. **18**(1): p. e2181192.

22. Willner, R., et al., *Potential and challenges of additive manufacturing for topology optimized spacecraft structures.* Journal of Laser Applications, 2020. **32**(3).

23. Lamarche-Gagnon, M.-É., et al., *Additively manufactured conformal cooling channels through topology optimization.* Structural and Multidisciplinary Optimization, 2024. **67**(8): p. 138.

24. Tyflopoulos, E., M. Lien, and M. Steinert, *Optimization of Brake Calipers Using Topology Optimization for Additive Manufacturing.* Applied Sciences, 2021. **11**(4): p. 1437.

25. Scarpellini, A., et al., *Laser Powder Bed Fusion of a Topology Optimized and Surface Textured Rudder Bulb with Lightweight and Drag-Reducing Design.* Journal of Marine Science and Engineering, 2021. **9**(9): p. 1032.

26. Brenner, S., et al., *Recoater crashes during powder bed fusion of metal with laser beam: simulative prediction of interference and experimental evaluation of resulting part quality.* Progress in Additive Manufacturing, 2023. **8**(4): p. 759-768.

27. Bartsch, K. and C. Emmelmann, *Enabling Cost-Based Support Structure Optimization in Laser Powder Bed Fusion of Metals.* JOM, 2022. **74**(3): p. 1126-1135.

28. Makeen, R., et al., *Distortion prediction and geometry compensation using modified inherent strain method for additively manufactured Ti-6Al-4V.* Journal of Manufacturing Processes, 2024. **131**: p. 1334-1347.

29. Levkulich, N.C., et al., *The effect of process parameters on residual stress evolution and distortion in the laser powder bed fusion of Ti-6Al-4V.* Additive Manufacturing, 2019. **28**: p. 475-484.

30. Bresson, Y., et al., *Global-to-local simulation of the thermal history in the laser powder bed fusion process based on a multiscale finite element approach.* The International Journal of Advanced Manufacturing Technology, 2023. **127**(9): p. 4727-4744.

31. Hocker, S.J., et al. *Additive Manufacturing Model-Based Process Metrics: Reduced Order Modeling of the Laser Powder Bed Fusion Process*. in *Materials Science and Technology, Technical Meeting and Exibition 2022*. 2022.

32. Kavas, B., et al., *Layer-to-layer closed-loop feedback control application for inter-layer temperature stabilization in laser powder bed fusion.* Additive Manufacturing, 2023. **78**: p. 103847.

33. Wang, Q., et al., *Model-based feedforward control of laser powder bed fusion additive manufacturing.* Additive Manufacturing, 2020. **31**: p. 100985.

34. Narasimharaju, S.R., et al., *A comprehensive review on laser powder bed fusion of steels: Processing, microstructure, defects and control methods, mechanical properties, current challenges and future trends.* Journal of Manufacturing Processes, 2022. **75**: p. 375-414.

35. Hong, G., et al. *Multi-Scale Model Predictive Control for Laser Powder Bed Fusion Additive Manufacturing*. in *ASME 2024 International Design Engineering Technical Conferences and Computers and Information in Engineering Conference*. 2024.

36. Vasileska, E., et al., *A novel paradigm for feedback control in LPBF: layer-wise correction for overhang structures.* Advances in Manufacturing, 2022. **10**(2): p. 326-344.

37. Riensche, A., et al., *Feedforward control of thermal history in laser powder bed fusion: Toward physics-based optimization of processing parameters.* Materials & Design, 2022. **224**: p. 111351.

38. Phan, M.A.L., O. Dew, and I. Todd, *Predictive process diagram for parameters selection in laser powder bed fusion to achieve high-density and low-cracking built parts.* Additive Manufacturing, 2024. **85**: p. 104145.

39. Druzgalski, C.L., et al., *Process optimization of complex geometries using feed forward control for laser powder bed fusion additive manufacturing.* Additive Manufacturing, 2020. **34**: p. 101169.

40. Yeung, H., B. Lane, and J. Fox, *Part geometry and conduction-based laser power control for powder bed fusion additive manufacturing.* Additive Manufacturing, 2019. **30**: p. 100844.

41. Kusano, M. and M. Watanabe, *Controlling heat accumulation through changing time per layer in laser powder bed fusion of nickel-based superalloy.* Journal of Manufacturing Processes, 2024. **131**: p. 187-198.

42. Johansson, T. *TJ2*. 2013; Available from: https://grabcad.com/library/tj2-1.

43. Carter, W.E., D.; Abbott, D.; Bruck, C.; Wilson, G.; Wolfe, J.; Finkhousen, D.; Tepper, A; Stevens, R.;, *The GE aircraft engine bracket challenge: An experiment in crowdsourcing for mechanical design concepts.* In Proceedings of the 25th Annual International Solid Freeform Fabrication Symposium, 2014: p. 4-6.

44. Marques, A., et al., *Inconel 718 produced by laser powder bed fusion: an overview of the influence of processing parameters on microstructural and mechanical properties.* The International Journal of Advanced Manufacturing Technology, 2022. **121**(9): p. 5651-5675.

45. Cole, K.D., M.R. Yavari, and P.K. Rao, *Computational heat transfer with spectral graph theory: Quantitative verification.* International Journal of Thermal Sciences, 2020. **153**: p. 106383.

46. Deshmukh, K., et al., *Effect of processing parameters and thermal history on microstructure evolution and functional properties in laser powder bed fusion of 316L.* Materials & Design, 2024. **244**: p. 113136.

47. Reza Yavari, M., et al., *Thermal Modeling in Metal Additive Manufacturing Using Graph Theory: Experimental Validation With Laser Powder Bed Fusion Using In Situ Infrared Thermography Data.* Journal of Manufacturing Science and Engineering, 2020. **142**(12).

48. Riensche, A.R., et al., *Predicting meltpool depth and primary dendritic arm spacing in laser powder bed fusion additive manufacturing using physics-based machine learning.* Materials & Design, 2024. **237**: p. 112540.

49. Yavari, R., et al., *Thermal modeling in metal additive manufacturing using graph theory – Application to laser powder bed fusion of a large volume impeller.* Additive Manufacturing, 2021. **41**: p. 101956.

50. Chetty, P., *Satellite technology and its applications*. 2023: Notion Press.

51. Dahmen, T., *Additive Manufacturing for Fuel Injectors: Design, Processes and Materials*, T.U.o. Denmark, Editor. 2021.

52. Bangalore Venkatesh, P., et al., *Pulse Performance Analysis of a 45 Newton Additively Manufactured Bipropellant Thruster.* Journal of Propulsion and Power, 2021. **37**(6): p. 832-841.

53. Gradl, P.R., et al. *Additive manufacturing of liquid rocket engine combustion devices: a summary of process developments and hot-fire testing results*. in *2018 Joint propulsion conference*. 2018.

54. Venturi, F. and R. Taylor, *Additive Manufacturing in the Context of Repeatability and Reliability.* Journal of Materials Engineering and Performance, 2023. **32**(15): p. 6589-6609.

55. Chen, Z., X. Wu, and C.H.J. Davies, *Process variation in Laser Powder Bed Fusion of Ti-6Al-4V.* Additive Manufacturing, 2021. **41**: p. 101987.

56. Schwerz, C., et al., *Increasing productivity of laser powder bed fusion manufactured Hastelloy X through modification of process parameters.* Journal of Manufacturing Processes, 2022. **78**: p. 231-241.

57. Agrawal, A.K., B. Rankouhi, and D.J. Thoma, *Predictive process mapping for laser powder bed fusion: A review of existing analytical solutions.* Current Opinion in Solid State and Materials Science, 2022. **26**(6): p. 101024.

58. Shkoruta, A., S. Mishra, and S.J. Rock, *Real-Time Image-Based Feedback Control of Laser Powder Bed Fusion.* ASME Letters in Dynamic Systems and Control, 2021. **2**(2).

59. Park, B., A. Chen, and S. Mishra, *Real-Time Melt Pool Homogenization Through Geometry-Informed Control in Laser Powder Bed Fusion Using Reinforcement Learning.* IEEE Transactions on Automation Science and Engineering, 2025. **22**: p. 2986-2997.

60. Rezaeifar, H. and M. Elbestawi, *Porosity formation mitigation in laser powder bed fusion process using a control approach.* Optics & Laser Technology, 2022. **147**: p. 107611.

61. Irwin, J.E., et al., *Iterative simulation-based techniques for control of laser powder bed fusion additive manufacturing.* Additive Manufacturing, 2021. **46**: p. 102078.

62. Shkoruta, A., B. Park, and S. Mishra, *An Empirical Model and Feedforward Control of Laser Powder Bed Fusion.* ASME Letters in Dynamic Systems and Control, 2024. **3**(4).

63. Yeung, H., et al., *Implementation of Advanced Laser Control Strategies for Powder Bed Fusion Systems.* Procedia Manufacturing, 2018. **26**: p. 871-879.

64. Ogoke, F. and A.B. Farimani, *Thermal control of laser powder bed fusion using deep reinforcement learning.* Additive Manufacturing, 2021. **46**: p. 102033.

65. Yao, D., et al., *Thermal behavior and control during multi-track laser powder bed fusion of 316 L stainless steel.* Additive Manufacturing, 2023. **70**: p. 103562.

66. Liao-McPherson, D., et al., *Layer-to-Layer Melt Pool Control in Laser Powder Bed Fusion.* IEEE Transactions on Control Systems Technology, 2025. **33**(1): p. 207-218.

67. Ren, Y., et al., *Control of interlayer temperature through laser power optimization in powder bed fusion.* Journal of Manufacturing Processes, 2025. **135**: p. 189-203.

68. Reiff, C., et al., *Learning Feedforward Control for Laser Powder Bed Fusion.* Procedia CIRP, 2021. **96**: p. 127-132.

69. Gordon, J.V., et al., *Defect structure process maps for laser powder bed fusion additive manufacturing.* Additive Manufacturing, 2020. **36**: p. 101552.

70. du Plessis, A., *Effects of process parameters on porosity in laser powder bed fusion revealed by X-ray tomography.* Additive Manufacturing, 2019. **30**: p. 100871.

71. *AmScope MU Series 10.0MP USB 3.0 Color CMOS C-Mount Microscope Camera with Reduction Lens*. 2025; Available from: https://amscope.com/products/mu1003.

72. Smith, B.A., et al., *The Interplay of Geometric Defects and Porosity on the Mechanical Behavior of Additively Manufactured Components.* Experimental Mechanics, 2021. **61**(4): p. 685-698.

73. Dimopoulos, A., et al., *Multi-Response Optimization of Ti6Al4V Support Structures for Laser Powder Bed Fusion Systems.* Journal of Manufacturing and Materials Processing, 2023. **7**(1): p. 22.

74. Lu, X., et al., *Recoater-Induced Distortions and Build Failures in Selective Laser Melting of Thin-Walled Ti6Al4V Parts.* Journal of Manufacturing and Materials Processing, 2023. **7**(2): p. 64.

75. *Artec Micro: Desktop 3D scanner*. 2025 [cited 2025 4/16/2025]; Available from: https://www.imakr.com/artec-3d/3462-artec-micro?srsltid=AfmBOooYvNrKzckLw6qTIFvbIPfSzNj0RiKkUqed3V9Mojkttp5rpY4H.

76. *CloudCompareWiki*. Available from: https://www.cloudcompare.org/doc/wiki/index.php/Main_Page.

77. Kobir, M.H., et al., *Prediction of recoater crash in laser powder bed fusion additive manufacturing using graph theory thermomechanical modeling.* Progress in Additive Manufacturing, 2023. **8**(3): p. 355-380.

78. Ulbricht, A., et al., *Can Potential Defects in LPBF Be Healed from the Laser Exposure of Subsequent Layers? A Quantitative Study.* Metals, 2021. **11**(7): p. 1012.

79. Gouge, M., et al., *Experimental validation of thermo-mechanical part-scale modeling for laser powder bed fusion processes.* Additive Manufacturing, 2019. **29**: p. 100771.

80. Mohammadtaheri, H., R. Sedaghati, and M. Molavi-Zarandi, *Inherent strain approach to estimate residual stress and deformation in the laser powder bed fusion process for metal additive manufacturing—a state-of-the-art review.* The International Journal of Advanced Manufacturing Technology, 2022. **122**(5): p. 2187-2202.

81. Zhao, C., et al., *Real-time monitoring of laser powder bed fusion process using high-speed X-ray imaging and diffraction.* Scientific Reports, 2017. **7**(1): p. 3602.

82. Wang, J., et al., *Understanding melt pool characteristics in laser powder bed fusion: An overview of single- and multi-track melt pools for process optimization.* Advanced Powder Materials, 2023. **2**(4): p. 100137.

83. Mukherjee, T., et al., *Printability of alloys for additive manufacturing.* Scientific Reports, 2016. **6**(1): p. 19717.

84. Cook, P.S. and D.J. Ritchie, *Determining the laser absorptivity of Ti-6Al-4V during laser powder bed fusion by calibrated melt pool simulation.* Optics & Laser Technology, 2023. **162**: p. 109247.

85. Zhang, S., et al., *On thermal properties of metallic powder in laser powder bed fusion additive manufacturing.* Journal of manufacturing processes, 2019. **47**: p. 382-392.

86. Li, X., et al., *Effects of temperature and strain rate on tensile properties and dynamic strain aging behaviour of LPBF Hastelloy X.* Additive Manufacturing Letters, 2023. **4**: p. 100105.

87. Tang, M. and P.C. Pistorius, *Anisotropic Mechanical Behavior of AlSi10Mg Parts Produced by Selective Laser Melting.* JOM, 2017. **69**(3): p. 516-522.

88. Deisenroth, D.C., et al., *Measurement Uncertainty of Surface Temperature Distributions for Laser Powder Bed Fusion Processes.* J Res Natl Inst Stand Technol, 2021. **126**: p. 126013.

89. Asgari, H., et al., *On thermal expansion behavior of invar alloy fabricated by modulated laser powder bed fusion.* Materials & Design, 2018. **160**: p. 895-905.

90. Tanrikulu, A.A., et al., *In Situ Microstructure Modification Using a Layerwise Surface-Preheating Laser Scan of Ti-6Al-4V during Laser Powder Bed Fusion.* Materials, 2024. **17**(8): p. 1929.

91. Jo, H., et al., *Spectral emissivity of oxidized and roughened metal surfaces.* International Journal of Heat and Mass Transfer, 2017. **115**: p. 1065-1071.

92. *Curve Fitting Toolbox*. 2024, MATLAB.

93. Sabzi, H.E., et al., *Controlling crack formation and porosity in laser powder bed fusion: Alloy design and process optimisation.* Additive Manufacturing, 2020. **34**: p. 101360.

94. Smith, C., et al., *Assessing Volumetric Energy Density as a Predictor of Defects in Laser Powder Bed Fusion 316L Stainless Steel.* JOM, 2025. **77**(2): p. 737-748.

95. Chen, X., et al., *Unveiling the layer-wise dynamics of defect evolution in laser powder bed fusion: Insights for in-situ monitoring and control.* Additive Manufacturing, 2024. **94**: p. 104414.

96. Moran, T.P., et al., *Spatial inhomogeneity of build defects across the build plate in laser powder bed fusion.* Additive Manufacturing, 2021. **47**: p. 102333.